Title
Variability of submicron aerosol observed at a rural site in Beijing in the summer of 2006

Journal
Journal of Geophysical Research Atmospheres, 114(7)

ISSN
0148-0227

Authors
Takegawa, N
Miyakawa, T
Kuwata, M
et al.

Publication Date
2009-04-16

DOI
10.1029/2008JD010857

Variability of submicron aerosol observed at a rural site in Beijing in the summer of 2006

N. Takegawa,[1] T. Miyakawa,[1] M. Kuwata,[1] Y. Kondo,[1] Y. Zhao,[2] S. Han,[1] K. Kita,[3] Y. Miyazaki,[4] Z. Deng,[5] R. Xiao,[5] M. Hu,[5] D. van Pinxteren,[6] H. Herrmann,[6] A. Hofzumahaus,[7] F. Holland,[7] A. Wahner,[7] D. R. Blake,[8] N. Sugimoto,[9] and T. Zhu[5]

Received 28 July 2008; revised 9 December 2008; accepted 21 January 2009; published 2 April 2009.

[1] Ground-based measurements of aerosol and trace gases were conducted at a rural site in Beijing in the summer of 2006 as a part of the Campaigns of Air Quality Research in Beijing and Surrounding Region 2006 (CAREBeijing 2006). The size-resolved chemical composition of submicron aerosol was measured using an Aerodyne quadrupole aerosol mass spectrometer (AMS). The data obtained from 15 August to 10 September 2006 are presented. Meteorological analysis shows that the measurement period can be characterized as a cycle of low wind speed periods over the course of a few days (stagnant periods) followed by rapid advection of clean air from the north/northwest mostly due to passage of a midlatitude cyclone. Mass concentrations of total measured aerosol with diameters less than 1 μm (total PM_1), which is defined as the sum of elemental carbon and nonrefractory components measured by the AMS, were highly variable, ranging from $\sim$2 to $\sim$100 $\mu g\,m^{-3}$. Large variability of the PM_1 composition and drastic changes in the sulfate (SO_4^{2-}) size distribution were observed to be associated with the cycle of stagnant periods and advection of clean air, indicating that both chemical and physical properties of aerosols were significantly altered on a time scale of a few days. We have found the dominance of organic aerosol at lower total PM_1 mass loadings and that of SO_4^{2-} at higher mass loadings, which may have important implications for the PM control strategy in Beijing. Possible factors affecting the evolution of the mass concentration and size distribution of SO_4^{2-} are discussed.

Citation: Takegawa, N., et al. (2009), Variability of submicron aerosol observed at a rural site in Beijing in the summer of 2006, *J. Geophys. Res.*, *114*, D00G05, doi:10.1029/2008JD010857.

1. Introduction

[2] Aerosol particles, which are emitted and formed from both anthropogenic and natural sources, play an important role in the atmosphere. High concentrations of aerosol in urban areas cause adverse effects on human health [*Dockery et al.*, 1993]. Aerosol particles scatter and absorb solar visible radiation and also act as cloud condensation nuclei (CCN), and these effects can significantly alter the radiative balance of the Earth's atmosphere [*Charlson et al.*, 1992; *Chung and Seinfeld*, 2002]. Fine-mode particles, which are defined as particles with aerodynamic diameters less than 2.5 μm ($PM_{2.5}$) or 1 μm (PM_1), consist mainly of anthropogenic compounds in continental regions [e.g., *NARSTO*, 2004]. Fine-mode particles are important because of their high deposition efficiency in the human respiratory system [*Dockery et al.*, 1993] and because of their large contributions to aerosol optical depth (AOD) in highly polluted regions [*Ramanathan et al.*, 2007].

[3] The Great North China Plain, which includes major megacities such as Beijing and Tianjin, is a large source of anthropogenic aerosol and its precursors [*Streets et al.*, 2003]. Satellite sensors such as the Moderate Resolution Imaging Spectroradiometer (MODIS), Multiangle Imaging Spectroradiometer (MISR), and Scanning Imaging Absorption Spectrometer for Atmospheric Chartography (SCIAMACHY) have revealed very large AOD and high concentrations of pollutants over wide areas of the Great North China Plain in recent years [*Bellouin et al.*, 2005; *Richter et al.*, 2005; *van Donkelaar et al.*, 2006]. Large amounts of aerosol and its precursors exported from this region can have significant impacts on air quality and climate both on regional and global scales, and thus the formation and physical/chemical transformation of aerosols occurring in this region need to be well understood.

[1] Research Center for Advanced Science and Technology, University of Tokyo, Tokyo, Japan.
[2] Air Quality Research Center, University of California, Davis, California, USA.
[3] Department of Environmental Science, Ibaraki University, Ibaraki, Japan.
[4] Institute of Low Temperature Science, Hokkaido University, Sapporo, Japan.
[5] College of Environmental Sciences, Peking University, Beijing, China.
[6] Leibniz Institute for Tropospheric Research, Leipzig, Germany.
[7] Forschungszentrum Jülich GmbH, Julich, Germany.
[8] Department of Chemistry, University of California, Irvine, California, USA.
[9] National Institute for Environmental Studies, Tsukuba, Japan.

0148-0227/09/2008JD010857

[4] There have been a substantial number of ground-based aerosol measurements at urban and suburban sites in Beijing [e.g., *Yao et al.*, 2003a, 2003b; *Duan et al.*, 2004, 2006; *Zheng et al.*, 2005; *Wang et al.*, 2006; *Guinot et al.*, 2007]. These measurements have provided useful insights into the average chemical compositions of $PM_{2.5}/PM_{10}$ aerosol and their seasonal variations. Sulfate and organic matter were found to be the major components of $PM_{2.5}$ aerosol in all seasons. Contributions of mineral dust to $PM_{2.5}$ mass were also important, especially in springtime. On the other hand, these measurements were mostly based on discrete sampling with relatively long integration times (from 24 h to several days), and thus hourly-to-daily variations of aerosol composition and size in Beijing have been poorly understood. Recent studies performed in the United States, Japan, and Mexico have shown that the chemical composition of fine particles could be significantly altered on a time scale of hours to days in regions strongly affected by anthropogenic sources [*de Gouw et al.*, 2005; *Takegawa et al.*, 2006a; *Volkamer et al.*, 2006; *Brock et al.*, 2008]. These studies suggest the importance of highly time-resolved measurements in investigating formation and transformation processes of aerosol near anthropogenic source regions.

[5] The Campaigns of Air Quality Research in Beijing and Surrounding Region 2006 (CAREBeijing 2006) was conducted in the summer of 2006. This is a joint project of China, Germany, United States, Korea, and Japan and is organized by Peking University (PKU). Intensive measurements were made at an urban site (PKU site) and a rural site (Yufa site). CAREBeijing 2006 was designed to identify the sources of ozone (O_3) and aerosols in Beijing and its surrounding regions to achieve better air quality during the Beijing Olympic Games in 2008. In addition to this main target, the CAREBeijing 2006 campaign provides a unique opportunity to investigate the formation and transformation processes of aerosol in Beijing. An Aerodyne quadrupole aerosol mass spectrometer (Q-AMS) [*Jayne et al.*, 2000] was deployed at the Yufa site. Hereafter the Q-AMS is simply referred to as the AMS. Considering the scientific importance of highly time-resolved measurements as mentioned above, the AMS has a great advantage compared to the previously reported off-line measurements because it can measure hourly variations of size-resolved chemical composition of submicron aerosols. Although *Zhang et al.* [2007] presented some AMS data obtained in Beijing, no detailed description of the AMS measurements in China has been published. A number of instruments measuring aerosol composition, aerosol physical and chemical properties, trace gases, and photolysis frequencies, were also deployed at the Yufa site. The major purpose of this paper is to investigate the variability of submicron aerosol observed at the Yufa site and its relation to meteorological conditions. Specifically, we focus on changes in the mass concentrations and size distributions of sulfate (SO_4^{2-}) by regional-scale processing.

2. Measurements

2.1. Yufa Site

[6] The Yufa site is a four-story building on the campus of Beijing HuangPu University (39°31′N, 116°18′E), which is located in a rural area ~53 km south of the PKU site. A major highway (Jingkai highway, connecting Beijing and Yufa from north to south) is located ~1.2 km east of the Yufa site. There are some small factories ~1 km south of the site. Possible effects of local emission sources will be discussed in section 4.1.

[7] The instruments of the University of Tokyo (UT) group were installed in a room located on the third floor of the building. In addition to the Aerodyne AMS, the chemical species measured in this room included elemental and organic carbon aerosol (EC and OC), carbon monoxide (CO), carbon dioxide (CO_2), reactive nitrogen species (NO, NO_2, and NO_y), and ozone (O_3). The room temperature was kept at 24°−28°C (depending on ambient dew point). Care was taken to keep the room temperature higher than the ambient dew point throughout the measurement period to avoid condensation of water vapor.

[8] The instruments of the PKU group were installed in a room located on the 4th floor. We use sulfur dioxide (SO_2) data obtained in this room. The room temperature was kept at 24°−26°C, which was sometimes lower than or close to the ambient dew point before 28 August 2006. Therefore, only data obtained after 29 August 2006 are used for the present analysis.

[9] Sample air was aspirated from the rooftop of the building for each instrument. The AMS was operated from 16 August to 9 September. In this study the measurement period is defined as the time between 15 August and 10 September so as to fully cover the AMS operation period. The mass concentrations of aerosol species are reported in units of $\mu g\ m^{-3}$ at 25°C and 1 atm. The time represents the Chinese local time (GMT + 0800) unless otherwise noted.

2.1.1. Aerodyne AMS

[10] Size-resolved mass concentrations of nonrefractory (vaporized at 600°C under vacuum) SO_4^{2-}, nitrate (NO_3^-), chloride (Cl^-), ammonium (NH_4^+), and organic matter (OM) were measured using an Aerodyne AMS by the UT group. The particle sizing by AMS is based on the vacuum aerodynamic diameter (d_{va}) [*DeCarlo et al.*, 2004]. The diameters measured by our AMS represent dry diameters because the sample air was dried before introduction into the AMS, as described later. The aerodynamic lens of the AMS allows particle transmission efficiencies of ~100% for d_{va} = 50–600 nm, with some transmission for $d_{va} > 1\ \mu m$, which is roughly similar to the commonly used PM_1 cutoff [*Jayne et al.*, 2000; *Takegawa et al.*, 2009]. Therefore, the aerosols measured by the AMS are referred to as nonrefractory PM_1 (NR-PM_1) aerosols. The integration time of the measurements was 10 min. Configuration of our AMS was basically the same as that presented by *Takegawa et al.* [2005]. Details of the performance of our AMS during the CAREBeijing campaign, including interpretation of mass spectra and particle collection efficiency (CE), were given by *Takegawa et al.* [2009]. Here we briefly describe the quality assessment of the AMS data.

[11] The sample air for the AMS was aspirated from the rooftop to the observation room using a stainless steel tube with an inner diameter (ID) of 10 mm and length of ~8.5 m (1/2-inch tube). Because of the relatively long sampling line and small sample flow rate of the AMS (~84 cc min^{-1}), an additional pump was used to draw air at ~10 L min^{-1} to reduce the residence time of air in the sampling line. A $PM_{2.5}$ cyclone (URG Corp., USA) was used to remove coarse particles. The 1/2-inch tube was reduced to a tube with an ID of

4.4 mm (1/4-inch tube) and subsequently to a tube with an ID of 2.0 mm (1/8-inch tube) using two isokinetic manifolds in order to match the AMS sample flow and orifice assembly. The total residence time of air in the sampling line was estimated to be ~5 s. The temperature of the 1/8-inch tube (length: ~0.49 m) and the AMS orifice was controlled at a constant value (40° or 42°C, depending on ambient dew point) to dry particles in the sample air, as we did for our Tokyo measurements [*Takegawa et al.*, 2005]. The relative humidity (RH) in the sample air was calculated to be < 44% for the entire period of the campaign. The rest of the inlet tube inside the room (length: ~0.33 m) was controlled at 30°C.

[12] Possible loss of aerosol particles through the relatively long sampling line was evaluated on the basis of simple aerodynamic calculations [*Hinds*, 1999]. The Reynolds number for the airflow in the 1/2-inch tube was ~1400, which indicates that the flow regime can be regarded as laminar. The aerodynamic properties of aerosol particles were calculated for particle diameters (d_p) of 0.05 and 0.5 μm, assuming the particle density of ammonium sulfate ($(NH_4)_2SO_4$: 1.77 g cm^{-3}). The impaction loss of the particles due to curvature of the inlet tube was estimated to be negligible (<0.1%) for the two selected diameters. The diffusion loss of the particles was also estimated to be small (~1% and ~0.1% for 0.05 and 0.5 μm, respectively).

[13] The limits of detection (LODs), which were estimated by placing a particle filter in the sample line (as was done by *Takegawa et al.* [2005]), were 0.1, 0.04, 0.02, 0.4, and 0.4 μg m^{-3} for SO_4^{2-}, NO_3^-, Cl^-, NH_4^+, and OM, respectively. The overall accuracy of the AMS measurements depends on the uncertainties in the ionization efficiency (IE), particle collection efficiency (CE), and approximation of the AMS size-cut to PM_1. The uncertainty in IE inferred from routine ammonium nitrate (NH_4NO_3) calibrations was estimated to be 18% using the same method as *Takegawa et al.* [2005]. The uncertainties in CE and AMS size-cut are more difficult to evaluate because these factors depend critically on the physical and chemical properties of aerosols in ambient air. At present there is no established way to determine CE by AMS data alone. The most reasonable way to assess the overall accuracy of the AMS measurements is to make an intercomparison with other independent measurements, as described in section 2.1.3.

2.1.2. Other Aerosol Instruments

[14] Mass concentrations of EC and OC were measured using a Sunset Laboratory semicontinuous EC/OC analyzer operated by the UT and PKU groups [*Kondo et al.*, 2006]. The time resolution was 1 h, including a sampling time of 40 min and an analysis time of 15 min. The sample line for the EC/OC analyzer was a stainless steel tube with an ID of 10 mm and a length of ~9 m. A PM_1 cyclone (URG Corp., USA) was used for the sampling inlet to match the size cut of the AMS. Ambient particles were collected on a quartz filter and then analyzed on the basis of the thermal-optical-transmittance method. The temperature protocol was based on that proposed by the National Institute for Occupational Safety and Health (NIOSH) [*Birch and Cary*, 1996]. A carbon denuder provided by the Sunset Laboratory was used to reduce the effects of volatile organic compounds (VOCs) on the OC measurements. The artifacts of VOCs, which were likely due to adsorption of VOCs on the quartz filter, were measured by placing a particle filter in the sample line. The OC concentrations were corrected by subtracting the VOC artifact from the measured OC concentrations (1.9 μgC m^{-3}). The accuracy of total carbon (TC = EC + OC) measurements is estimated to be ~7% based on sucrose calibration and routine methane (CH_4) calibration.

[15] Size-resolved mass concentrations of ionic compounds were measured using a five-stage Berner cascade impactor (Hauke, Austria). The Berner impactor sampler was installed on the rooftop of the observation building and operated by the Leibniz Institute for Tropospheric Research (IFT) group. The Berner impactor had cut points of 0.05, 0.14, 0.42, 1.2, 3.5, and 10 μm in transition/continuum regime aerodynamic diameter (d_a) at ambient RH. The sample flow rate was 75 L min^{-1} and the integration time ranged from 2.5 to 10 h. Preheated (2 h at 350°C) aluminum foils were used as sampling substrates. The aerosol samples were stored at −20°C and sent to Germany for chemical analysis. The analyzed parameters/species include total mass, major inorganic ions (SO_4^{2-}, NO_3^-, Cl^-, NH_4^+, Na^+, K^+, and Ca^{2+}), and others. Aliquots of the impactor foils were cut into small pieces and extracted in 1.5 mL deionized water (Nanopure, Barnstead, USA) by shaking and ultrasonication. After filtration through 0.45-μm pore size syringe filters (Acrodisc 13, Pall, USA), the extract was analyzed by a variety of techniques. Analysis of inorganic ions was carried out by ion chromatography (IC690, Metrohm, Switzerland). Analytical uncertainties are estimated to be ~10% for major ions. We use the sum of 0.05–0.14, 0.14–0.42, and 0.42–1.2 μm stages for intercomparison with the AMS.

2.1.3. Intercomparison of AMS With Other Instruments

[16] The AMS data were compared with the Berner impactor and EC/OC analyzer. Details of the intercomparisons were given by *Takegawa et al.* [2009], and only a summary of the intercomparison results is presented here. Previous studies have shown that an AMS CE = 0.5 is a good assumption in many cases, especially under dry conditions [e.g., *Allan et al.*, 2004; *Takegawa et al.*, 2005]. We assumed CE = 0.5 for preliminary intercomparison since we dried the sample air of the AMS, but we found that the AMS systematically overestimated the Berner impactor data by a factor of ~1.7 for SO_4^{2-}, Cl^-, and NH_4^+ and by a factor of ~1.2 for NO_3^-. The difference in the size-cut between the AMS and Berner impactor (including effects of ambient RH) does not explain the overestimation by the AMS, as explained below. The 50% cutoff diameters are d_{va} ~1 μm [*Takegawa et al.*, 2009] and d_a = 1.2 μm for the AMS and Berner impactor, respectively. A simple calculation based on the definition of aerodynamic diameter [*DeCarlo et al.*, 2004] indicates that the cutoff diameter of the AMS was smaller than that of the Berner impactor unless the ratio of particle density to dynamic shape factor (i.e., effective density) was smaller than 0.6, which is only the case for soot aggregates [*Park et al.*, 2003]. If we assume spherical $(NH_4)_2SO_4$ particles, d_{va} = 1 μm is equivalent to d_a = 0.78 μm. As for the effects of ambient RH, the ratio of the AMS SO_4^{2-} to Berner impactor SO_4^{2-} did not show systematic dependence on ambient RH, suggesting that the effects of ambient RH on the Berner impactor size-cut was not significant. This is probably because an increase in geometric diameter by hygroscopic growth was partially canceled by changes in effective density. In the following analysis, we assume CE = 1.0 for all species (SO_4^{2-}, NO_3^-,

Cl^-, NH_4^+, and OM), although the physical basis for this assumption has not been well identified. Because CE is smaller than or equal to unity, the mass concentrations reported here should be regarded as lower limits.

[17] The linear regression slopes of the AMS versus Berner impactor were found to be 0.86, 0.61, 0.83, and 0.87 for SO_4^{2-}, NO_3^-, Cl^-, and NH_4^+, respectively (r^2 = 0.87–0.93). Note that the regression lines were forced through the origin owing to the limited number of data points. As for SO_4^{2-}, Cl^-, and NH_4^+, the AMS tended to underestimate the Berner impactor by 13–17%, but the differences were comparable to the combined accuracies of the two measurements: 18% for the AMS (inferred from the routine calibrations) and 10% for the Berner impactor. On the other hand, the AMS underestimated the Berner impactor by ~40% for NO_3^-. Possible underestimation of NO_3^- due to the presence of refractory NO_3^- such as sodium nitrate ($NaNO_3$) and calcium nitrate ($Ca(NO_3)_2$) was likely minor in this case because of low concentrations of Na^+ (<0.6 μg m^{-3}) and Ca^{2+} (<0.5 μg m^{-3}) identified in the water extracts of the Berner impactor samples at 0.05–1.2 μm. A comparison of the size distributions of SO_4^{2-} and NO_3^- between the AMS and Berner impactor [*Takegawa et al.*, 2009] (plots are not shown here) suggested that the significant underestimation of NO_3^- by the AMS might have been due to the difference in the size cut between the AMS and Berner impactor. We interpret that the mass loadings between the AMS cutoff diameter (d_{va} ~ 1 μm) and Berner impactor cutoff diameter (d_a = 1.2 μm) was small (~14% at most) for SO_4^{2-} but significant (as large as ~40%) for NO_3^-. This implies externally mixtures of SO_4^{2-} and NO_3^- around this size range. The possibility of external mixtures of SO_4^{2-} and NO_3^- is further discussed in section 4.2.

[18] The AMS OM data were compared with the Sunset OC data. The regression slope and intercept of the AMS OM versus Sunset OC was found to be 1.99 and 0.79 μg m^{-3}, respectively (r^2 = 0.72). The slope was consistent with the OM/OC ratios of 1.6–2.1 given by *Turpin and Lim* [2001], supporting the plausibility of the assumption of CE = 1.0 for OM. The assumption of CE = 0.5 implies unrealistically high OM/OC ratios of as high as 4.

[19] Consequently, the accuracy of the PM_1 mass measurements by the AMS was estimated to be better than 20% for SO_4^{2-}, Cl^-, and NH_4^+ and ~40% for NO_3^- during the CARE-BEIJING campaign. We should note that the above error estimate relies on the intercomparison with the Berner impactor and Sunset OC measurements, and that the AMS in general has an uncertainty of as large as a factor of 2 as a standalone instrument, mostly due to the uncertainty in CE.

2.1.4. Gaseous Species and Meteorological Data

[20] Carbon monoxide was measured using a nondispersive infrared absorption (NDIR) instrument with an integration time of 1 min (Model 48, Thermo Environmental Instruments (TEI), USA.). Carbon dioxide was measured using an NDIR-based instrument with an integration time of 10 s (Model LI7000, Li-Cor, Inc., USA). The CO and CO_2 instruments used a common Teflon tube inlet from the rooftop (ID: 6 mm, length: ~10 m). The performances of the CO and CO_2 instruments were basically the same as those used for our previous measurements in Tokyo [*Takegawa et al.*, 2006b]. The only difference is that we used two sets of Nafion dryer systems (Perma-Pure Inc., USA) to achieve a better removal efficiency of water vapor in the sample air. Routine calibrations during the campaign were performed using CO and CO_2 standards manufactured by Beijing Hua Yuan Gas Chemical Industry, Co., Ltd., in China. The CO and CO_2 standards were prepared in aluminum cylinders and their nominal concentrations were 5 ppm by volume (ppmv) CO in air, 358 ppmv CO_2 in air, and 639 ppmv CO_2 in air. The nominal concentrations of the Chinese standard gases were calibrated (scaled) using CO and CO_2 standard gases manufactured by U.S. companies (Matheson Tri-Gas for CO and Airgass for CO_2) at the end of the campaign. The CO and CO_2 concentrations of the U.S. standards were 5.0 ppmv CO in air and 586 ppmv CO_2 in air. The difference between the Chinese and U.S. standards was 4% for CO and 3% for CO_2. The accuracy (excluding the accuracy of the U.S. standards) and precision of the CO measurements are estimated to be 1.4% and 4 parts per billion by volume (ppbv), respectively (at CO = 400 ppbv, 1 min), and those of the CO_2 measurements are estimated to be 0.2% and 0.3 ppmv, respectively (at CO_2 = 400 ppmv, 10 s). The CO_2 data before 25 August were largely missing owing to a problem in the data acquisition system.

[21] Reactive nitrogen species (NO, NO_2, and NO_y) were measured using an NO-O_3 chemiluminescence detector (Model 42CTL, TEI, USA) combined with a blue-light photolytic converter and a custom-made gold tube catalytic converter [*Kondo et al.*, 2008]. The sum of NO and NO_2 is referred to as NO_x. The NO_x and NO_y instruments were operated by the UT and Ibaraki University (IU) groups. The integration time of the NO_x and NO_y measurements was 1 min. Instead of using a long sample line from the rooftop, we used a thick, short Teflon pipe (ID: 46 mm, length: 2 m) that stuck out from the window in order to avoid possible loss of reactive compounds (especially nitric acid) in a long sample line. The air was aspirated at a flow rate of ~1200 L min^{-1} using a blower. This resulted in a short residence time of ~0.2 s but a high Reynolds number of ~36,000 (i.e., turbulent flow). A Teflon manifold (ID: 35 mm) with four branch ports (bored-through connectors for 1/4-inch Teflon tubes) was attached to the end of the Teflon pipe. The sample air of the NO_x and NO_y instruments was taken from the centerline of the manifold through the bored-through connectors to avoid wall effects. Routine calibrations of NO_x and NO_y during the campaign were performed using an NO standard (nominal concentration of 4 ppmv in N_2) manufactured by the Beijing Hua Yuan Gas Chemical Industry. The Chinese NO standard was calibrated with an NO standard from Matheson Tri-Gas at the end of the campaign. The sensitivity of a NO-O_3 chemiluminescence detector depends on RH in the sample air. The routine calibrations were made by mixing the NO standard with humidified zero air and also with ambient air. The resulting concentration of NO in the sample air was ~40 ppbv. Effects of RH on the NO sensitivity were ~8% and have been corrected in the data reduction. The background levels were measured by injecting humidified zero air into the sample line. The effects of humidity on the background were found to be negligible. The conversion efficiency of NO_2 to NO and that of NO_y to NO were ~30% and >95%, respectively, during the campaign. The accuracies of the NO, NO_2, and NO_y measurements were estimated to be 7%, 13%, and 12%, respectively, based on the uncertainties in the sample flow rates, conversion efficiencies,

and concentration of the NO standard. The LODs of the NO, NO_2, and NO_y measurements were estimated to be 0.15 ppbv, 0.5 ppbv, and 0.6 ppbv, respectively, based on the fluctuations of the background signals.

[22] O_3 was measured using a UV absorption technique by the UT-IU group (Model 49C, TEI, USA) [*Kondo et al.*, 2008] and Forschungszentrum Jülich GmbH (FZJ) group (Model O_3 41M, Environnement SA, France). The integration times were 1 min and 5 s for the UT-IU and FZJ measurements, respectively. The UT-IU O_3 instrument shared the short Teflon pipe inlet with the NO_x and NO_y instruments. The accuracy and precision of the UT-IU O_3 measurements are estimated to be 5% and 0.3 ppbv, respectively. The FZJ O_3 instrument was mounted in a laboratory field container, with air inlets at ~7 m above ground (FZJ container). The FZJ O_3 instrument was calibrated in Jülich against standard O_3 calibrators (Model O_3 41M, Environnement SA, France, and Model TE49C-PS, TEI, USA). The accuracy and precision of the FZJ O_3 measurements are estimated to be <5% and 0.5 ppbv, respectively. The UT-IU O_3 instrument was operated from 13 to 27 August, and the FZJ O_3 instrument was operated from 19 August to 9 September. During the overlap period, the two O_3 measurements agreed well, within the combined uncertainties (linear regression slope = 0.95, intercept = 2.1 ppbv, $r^2 = 0.99$).

[23] Sulfur dioxide was measured by the PKU group using an ultraviolet (UV) fluorescence technique (Model EC9850B, ECOTECH, Australia) with an integration time of 1 min. As mentioned earlier, only data obtained after 29 August 2006 are used for the present analysis. The nominal accuracy and precision given by the manufacturer are 1% and 2% (at 5 min), respectively. However, the actual uncertainties have not been evaluated because routine calibrations were not performed during the measurement period (i.e., accuracy of the SO_2 data relies on the calibration factor provided by the manufacturer). On the basis of our previous experiments in Tokyo, a similar type of UV fluorescence SO_2 instrument (Model 43C, TEI, USA) showed a stable performance over the course of a year (variability of the calibration factor was within 5%) [*Miyakawa et al.*, 2007]. Here we assume that the accuracy of the SO_2 instrument used at the Yufa site was of the same order of magnitude (~5%) as that used in Tokyo, at least for the data obtained after 29 August 2006.

[24] Number concentrations of hydroxyl (OH) radical were measured using a laser-induced fluorescence (LIF) instrument, operated by the FZJ group. Details of the instrument and its calibration were reported by *Holland et al.* [2003], and only brief descriptions are given here. The OH instrument was mounted in the FZJ container. Ambient air was sampled continuously into a low-pressure detection chamber, where OH was detected by pulsed laser-excited fluorescence at a wavelength of 308 nm. The instrument was calibrated using the quantitative photolysis of water vapor in synthetic air at 185 nm as a radical source. The accuracy and precision of OH measurements are estimated to be 20% and 4×10^5 cm^{-3} (at OH = 2×10^6 cm^{-3}, 10 min), respectively.

[25] Measurements of volatile organic compounds (VOCs) and CO were conducted using a whole air sampling (WAS) technique by the University of California, Irvine (UCI) group [*Simpson et al.*, 2003]. Stainless-steel canisters were evacuated in the UCI laboratory and then shipped to China. Whole air samples were collected in the center of a field on the University campus (~100 m away from the building). The sampling was made by opening the canister valve for ~10 s (until the pressure in the canister became equal to the ambient pressure). The filled canisters were shipped back to the UCI laboratory for the chemical analysis. The precision and accuracy of the VOC measurements were basically the same as those given by *Simpson et al.* [2003]. The accuracy and precision of the WAS-CO measurements were 5% and 3%, respectively. The sampling was made mostly during daytime with a time interval of ~3 h.

[26] Surface meteorological parameters were measured on the rooftop of the four-story building using meteorological sensors (R. M. Young Company, Michigan, USA) operated by the PKU group. The meteorological sensors consisted of a Platinum resistance temperature detector (Model 41342), a capacitance-type RH sensor (Model 41382), and a wind sensor with helicoids propeller and vane (Model 05103).

2.2. Lidar Observation Site

[27] Vertical profiles of aerosol were measured using a two-wavelength (532 and 1064 nm) polarization (532 nm) lidar [*Sugimoto et al.*, 2002]. The lidar was installed at the Sino-Japan Friendship Center for Environmental Protection (39°59′N, 116°25′E), which is located ~10 km east of the PKU site and ~53 km north–northeast of the Yufa site. The lidar data were used to estimate the height of the mixed layer (ML) and cloud base. The concentrations of aerosol are generally high in the ML and low above the ML. The ML height can be determined from the falling edge of the lidar backscattering intensity. The ML height is defined here as the height where the normalized gradient of the attenuated backscatter coefficient at 1064 nm (absc1064) has a maximum. The cloud base height is defined as the height where the vertical gradient of absc1064 exceeded 4×10^{-8} m^{-2} sr^{-1} and the maximum value of absc1064 in the cloud layer exceeded 5×10^{-6} m^{-1} sr^{-1}. The estimates of the ML and cloud base heights are not available when the aerosol vertical structures were not well defined.

3. Characterization of Air Masses

3.1. Air Mass Origins

[28] General characteristics of the meteorological field during the campaign were investigated using data from the National Centers for Environmental Prediction (NCEP) (http://www.ncep.noaa.gov/). Large-scale meteorological patterns in East Asia can be characterized by the summer monsoon. Maritime air was generally transported from the western Pacific to the Asian continent. The average winds in the boundary layer (925 hPa) over the Great North China Plain were weak southerly during the measurement period (plots are not shown). Regarding day-to-day or weekly variations of meteorology during the measurement period, drastic changes in the flow patterns over northern China occurred on a time scale of several days mostly owing to passage of midlatitude cyclones.

[29] Two-day backward trajectories from the National Oceanic and Atmospheric Administration (NOAA) HYSPLIT model were used to investigate possible origins of the observed air masses. Trajectories were calculated for each day during the measurement period (from 16 August to 8 September 2006), with a starting time of 1200 GMT (2000 LT) and a

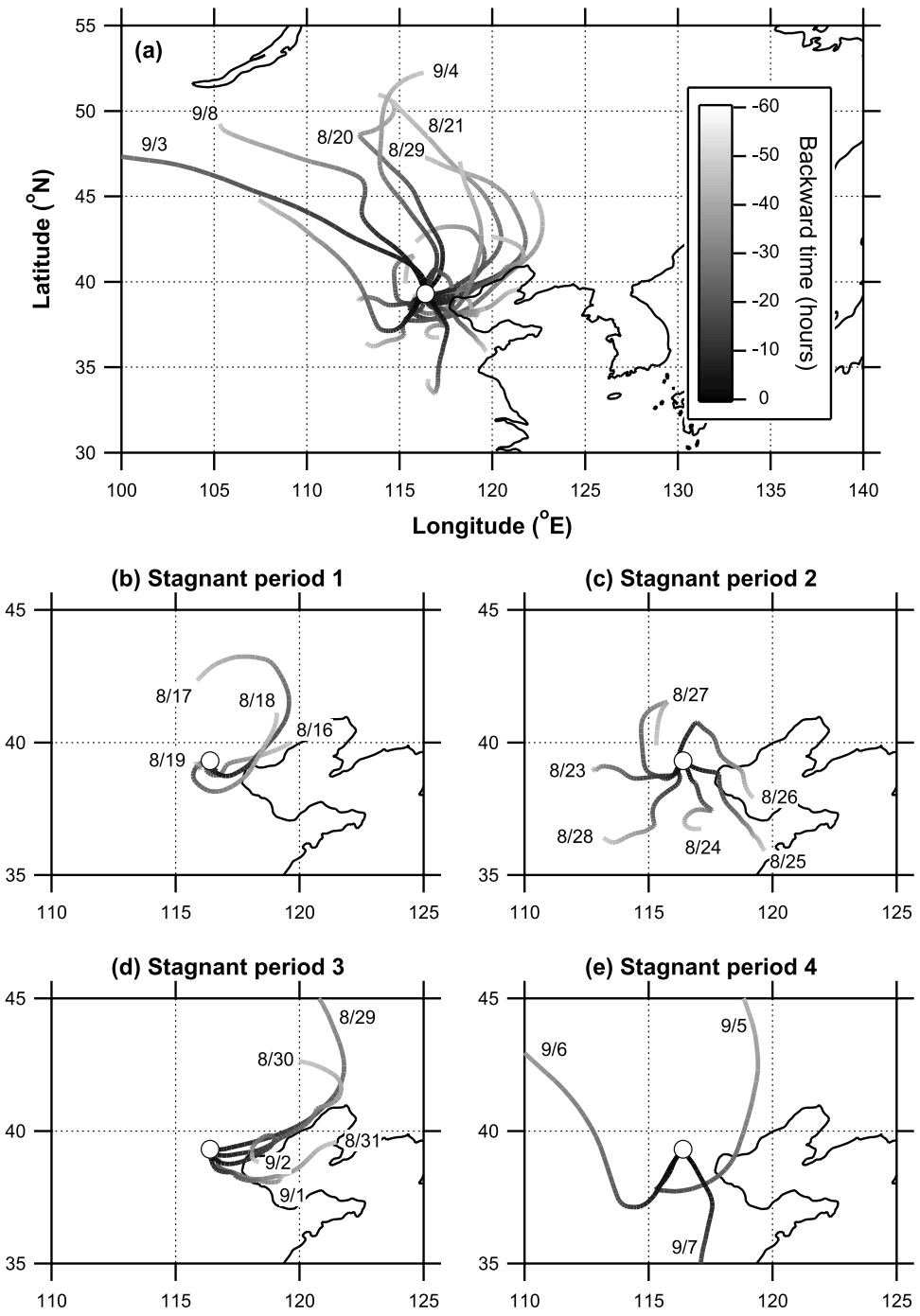

Figure 1. Two-day backward trajectories calculated using the NOAA HYSPLIT model. The trajectories were calculated for each day during the measurement period, with a starting time of 1200 GMT (2000 LT) and a starting altitude of 500 m above sea level. The open circle indicates the location of the Yufa site.

starting altitude of 500 m above sea level. The measurement period is classified into four stagnant periods based on the backward trajectories, as illustrated in Figure 1. There were some episodes of rapid advection of clean air (i.e., the trajectories traveling a longer distance in Figure 1a) between stagnant periods. The rapid advection of clean air on 20 August, 3 September, and 8 September was due to the passage of a midlatitude cyclone associated with a cold front (strong northerly winds over Beijing), while that on 29 August was not associated with the passage of cyclones but with a change in air mass origin. In each stagnant period, air masses were generally confined to within ~500 km distance from the site during the preceding 2 days.

[30] *Streets et al.* [2003] developed an emission inventory in Asia for the year 2000, and *Streets et al.* [2006] have recently updated the CO emissions from China. The Streets inventory for 2000 may be somewhat outdated to quantitatively interpret the CAREBEIJING data. Nevertheless, it includes more comprehensive information than the updated version and is still useful to investigate the categories of

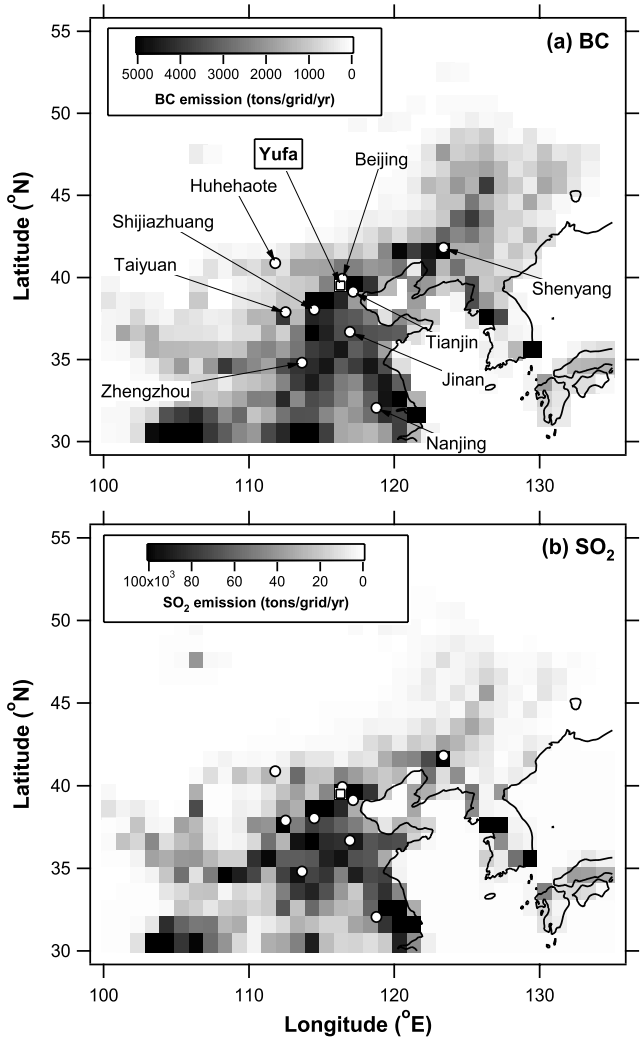

Figure 2. Map of (a) annual BC emissions (tons grid^{-1} a^{-1}) and (b) annual SO_2 emissions (tons grid^{-1} a^{-1}) produced from an emission inventory for the year 2000 [*Streets et al.*, 2003]. The open square and open circles show the locations of the Yufa site and major cities, respectively. Note that Yufa is a part of Beijing. "Beijing" in this map indicates the location of the center of Beijing city.

major emission sources and their geographic locations assuming that they have not changed significantly over 6 years. Figure 2 shows annual emissions of black carbon (BC) and SO_2 produced from the Streets inventory. Note that the terminology "BC" is based on the Streets definition. Apart from some differences between BC and EC, they can be regarded as the same in this context. Table 1 shows a summary of annual emissions of CO_2, CO, SO_2, BC, and OC in Beijing based on the Streets emission inventory. The categories of the emission sources include industry, domestic usage (coal/biofuel combustion), transportation, and power generation. Biomass burning, although it is not listed in Table 1, could be an important source of pollutants depending on seasons.

[31] In addition to the emission sources in Beijing, there are a large number of emission sources around the Yufa site, especially to the south of Beijing (Figure 2). Together with the backward trajectories shown above, it is suggested that the air masses observed at the Yufa site were significantly affected by various emission sources located within ~500 km of the site. It would be rather difficult to identify the major emission source during each stagnant period because polluted air masses from these various sources will have been mixed.

3.2. Surface Meteorological Data and Lidar Data

[32] Figures 3a and 3b show time series of air temperature, RH, wind speed, and wind direction observed at the Yufa site. Figures 3c and 3d show frequency distribution of wind speed and direction during the daytime (1000–1800 LT) and from evening to the following morning (1800–1000 LT), respectively. The classification of the local time is based on the average diurnal profile of wind speeds (not shown): the wind speeds tended to be higher at 1000–1800 LT. The absc1064 and the heights of ML and cloud bases estimated from the lidar measurements are displayed in Figures 4a and 4b, respectively. Precipitation was not monitored at the Yufa site. Alternatively, precipitation data at the Beijing airport (40°05′N, 116°35′E, ~67 km from the Yufa site) provided by the University of Wyoming (http://weather.uwyo.edu/surface/meteogram/) are plotted in Figure 4b.

[33] The passages of cyclones can also be identified from the surface meteorological data as they can be characterized by rapid changes in RH and/or wind speeds. During stagnant periods we observed high RH (>~90%) at night throughout the measurement period. This may be a favorable condition for the formation of cloud or fog droplets. In fact, the lidar measurements have detected frequent appearances of clouds at the top of ML. The MODIS data have also indicated that the Beijing region was mostly covered by low-level clouds during the measurement period (not shown). Together with the frequent appearance of low-level clouds, there were a few precipitation events during the measurement period (a few hours in duration on 25, 29, and 30 August and 3, 7, and 8 September).

4. Results

4.1. Combustion Tracers

[34] Temporal variations and correlations of combustion tracers (CO, CO_2, NO_x, EC, etc.) may provide some insight into emission sources in the Beijing region. Figures 5a and 5b show time series of CO, CO_2, NO_x/NO_y ratio, EC, *m*43, and *m*60 during the whole measurement period (10 August to 10 September). *m*43 (or *m*60) is the equivalent mass concentration of organic compounds represented by the signal intensity at *m*/*z* 43 (or *m*/*z* 60) in the AMS mass spectra [*Zhang et al.*, 2005a]. This definition is also applicable to other *m*/*z* peaks.

Table 1. Annual Emissions of Gaseous and Particulate Matters From Beijing for the Year 2000[a]

	Industry	Domestic	Transportation	Power
CO_2	28,450	10,175	10,295	17,978
CO	545	419	1,731	N/A
SO_2	124	58	7.6	169
BC	3.8	3.3	1.6	0.5
OC	0.7	9.4	1.4	0.4

[a]Unit is Gg a^{-1}. Data are from *Streets et al.* [2003].

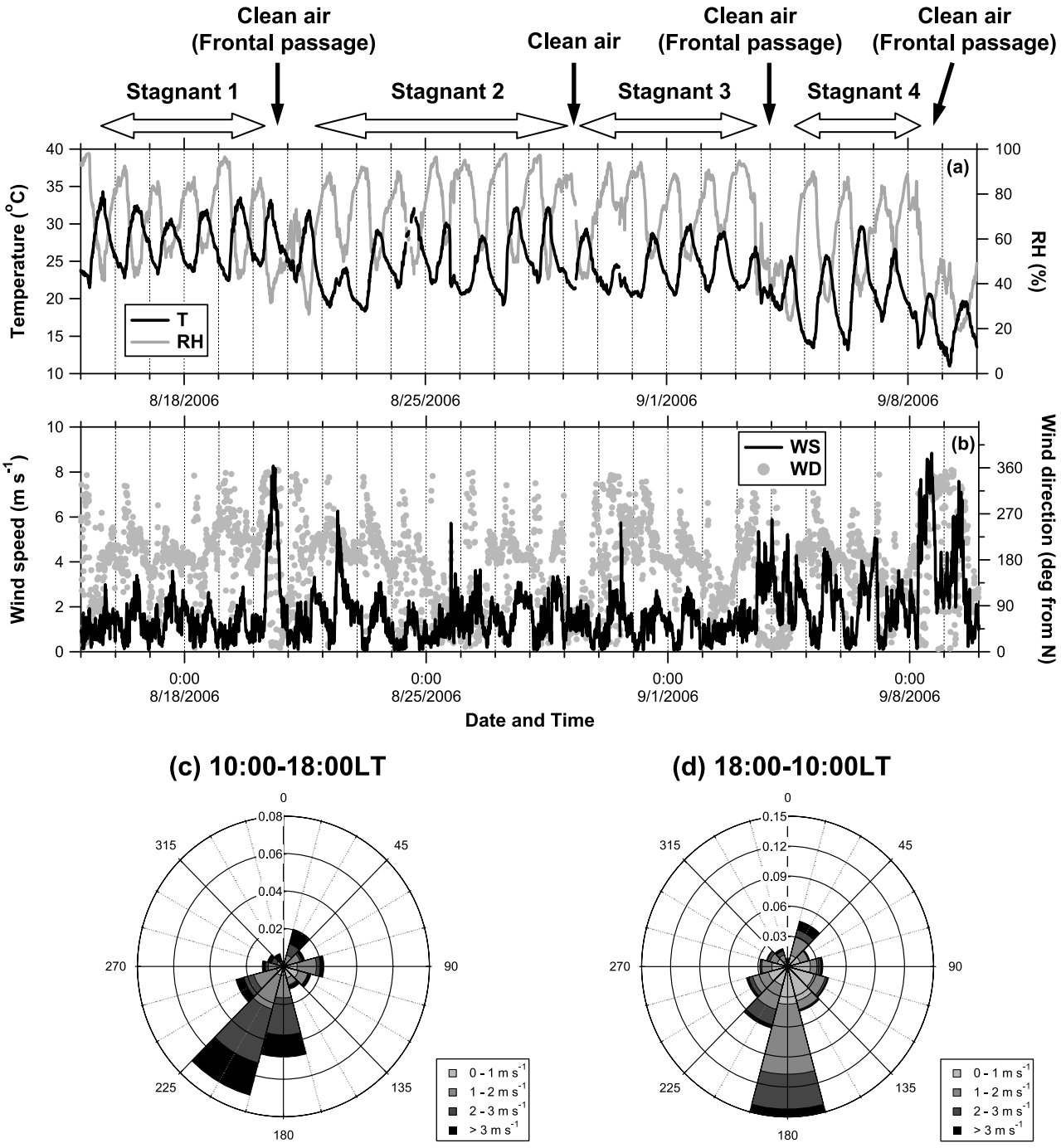

Figure 3. Time series of (a) air temperature (black line), relative humidity (RH: shaded line), (b) wind speed (black line), and wind direction (shaded circles) observed at the Yufa site. Frequency distribution of wind speed and direction during (c) the daytime (1000–1800 LT) and (d) from evening to the following morning (1800–1000 LT).

CO, CO_2, NO_x, and EC are emitted predominantly from combustion sources. Emission factors of these compounds depend on fuel and device type and combustion efficiency. The *m*43 is a mixture of hydrocarbon-like organic aerosol (both from combustion and noncombustion origins) and oxygenated organic aerosol [*Zhang et al.*, 2005a]. Although *m*57 may be more appropriate as a marker of hydrocarbon-like aerosol, we use *m*43 because of its better signal-to-noise ratio. Indeed, the temporal variation of *m*43 correlated well with that of *m*57 (r^2 = 0.72), suggesting that *m*/*z* 43 signals can be regarded as a good proxy for hydrocarbon-like aerosol in this case. *m*60 has been identified as a marker of wood burning organic aerosols [*Alfarra et al.*, 2007].

[35] The temporal variations of CO, CO_2, EC, *m*43, and *m*60 generally showed positive correlation but also exhibited different behaviors in certain cases. Specifically, the temporal

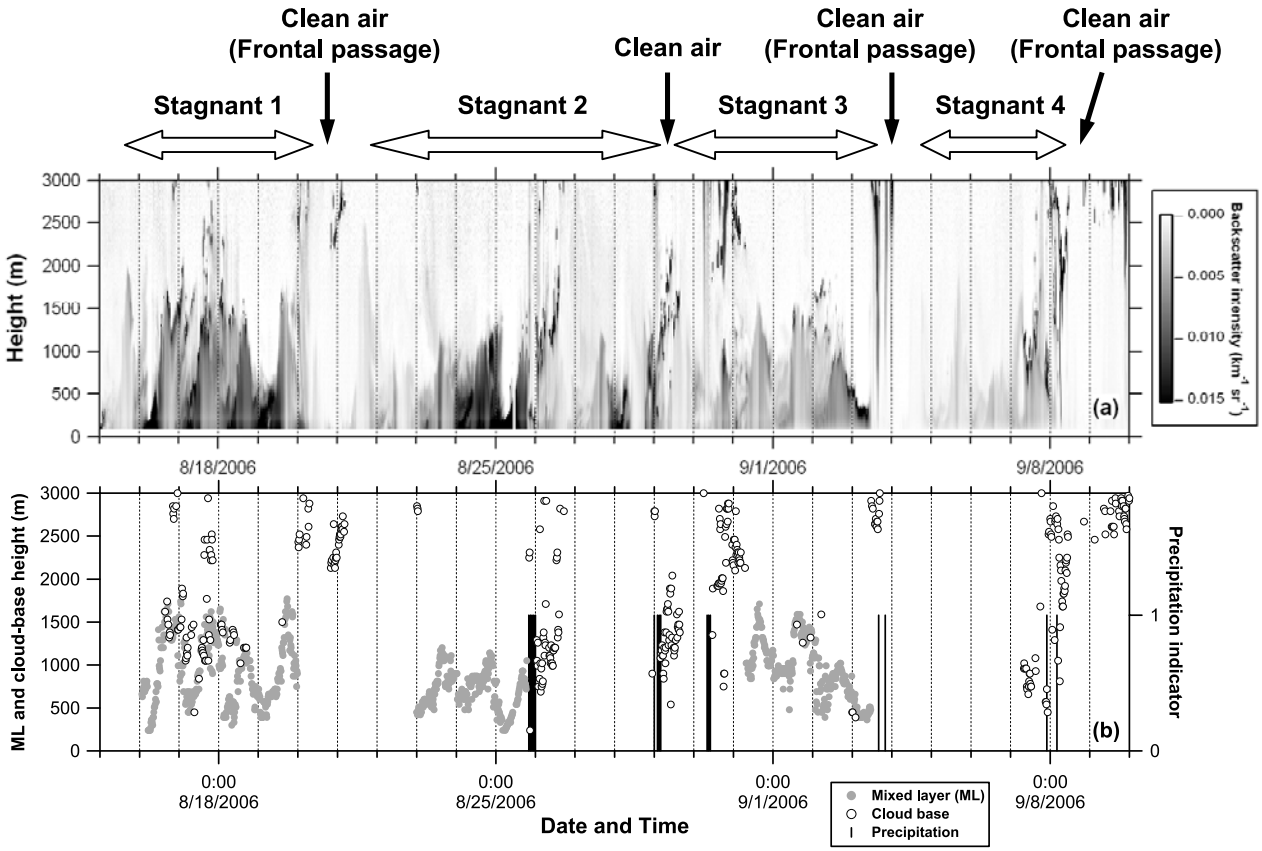

Figure 4. Time series of (a) attenuated backscatter coefficient at 1064 nm obtained by the lidar measurements and (b) heights of ML (shaded circles) and cloud base (open circles) estimated from the lidar measurements and precipitation indicator (solid line) obtained at the Beijing airport. Note that the precipitation indicator is qualitative (1: precipitation, 0: no precipitation) with 1-h time resolution.

variation of CO was significantly different from those of the other species. Interpretations are given below.

4.1.1. Influence of Local Sources

[36] Enhancement ratios of CO relative to CO_2 ($\Delta CO/\Delta CO_2$ ratios) can be used to characterize the types of emission sources (both anthropogenic and biomass burning), where Δ denotes the enhancement above the local background levels [*Takegawa et al.*, 2004, and references therein]. Large increases in CO_2 without significant changes in CO were observed almost every night. The very low $\Delta CO/\Delta CO_2$ ratios during the nighttime events indicate that these air masses were affected by high combustion efficiency sources. Respiration by vegetation may have been another contributor to the increase in CO_2 during nighttime, but it is unlikely that the enhancements of 100–200 ppmv were predominantly from vegetation. Simultaneous enhancements of EC (and NO_x, *m*43, etc.) during the nighttime events also suggest influences from combustion sources. Considering the high NO_x/NO_y ratios (0.8–1.0), low wind speeds, and low ML heights during nighttime, these enhancements were likely affected by local emission sources. Possible local sources were diesel emissions from the Jingkai highway located ~1.2 km east of the Yufa site. Although there is no available data for $\Delta CO/\Delta CO_2$ ratios from on-road vehicles in Beijing to the best of our knowledge, our measurements in Tokyo, where emissions were dominated by diesel/gasoline vehicles, indicate low $\Delta CO/\Delta CO_2$ ratios (~0.01) [*Takegawa et al.*, 2006b].

[37] Other evidence for local diesel emissions can be found in size distribution data. Figure 5c shows the size distributions of *m*43 during a large enhancement event in the early morning (0410–0650 LT) and during the daytime (1000–1800 LT) on 1 September. CO_2 and EC reached 626 ppmv and 15 μg m^{-3}, respectively, during the large enhancement event. The size distribution of *m*43 during this event showed bimodal peaks at d_{va} ~200 nm and ~500 nm. The peak diameter of the small-mode particles is similar to those found in many urban locations [*Allan et al.*, 2003; *Alfarra et al.*, 2004; *Zhang et al.*, 2005b, 2005c; *Takegawa et al.*, 2006b]. The presence of small-mode particles indicates that the aerosols were relatively fresh, because the contributions of small-mode particles tend to decrease in aged air [e.g., *Alfarra et al.*, 2004]. Conversely, the monomodal size distribution of *m*43 during the daytime suggests that the air masses were not largely affected by local emission sources.

[38] The average daytime size distributions of *m*43 on other days were similar to that on 1 September, except for the case of 29 August. Large spikes in *m*43 (and *m*57) that were not associated with increases in CO, CO_2, and EC were observed during the daytime on 29 August. The size distribution of *m*43 showed a distinct peak at d_{va} = 80–90 nm in some of these spikes (1000–1140 LT: Figure 5d), indicating that

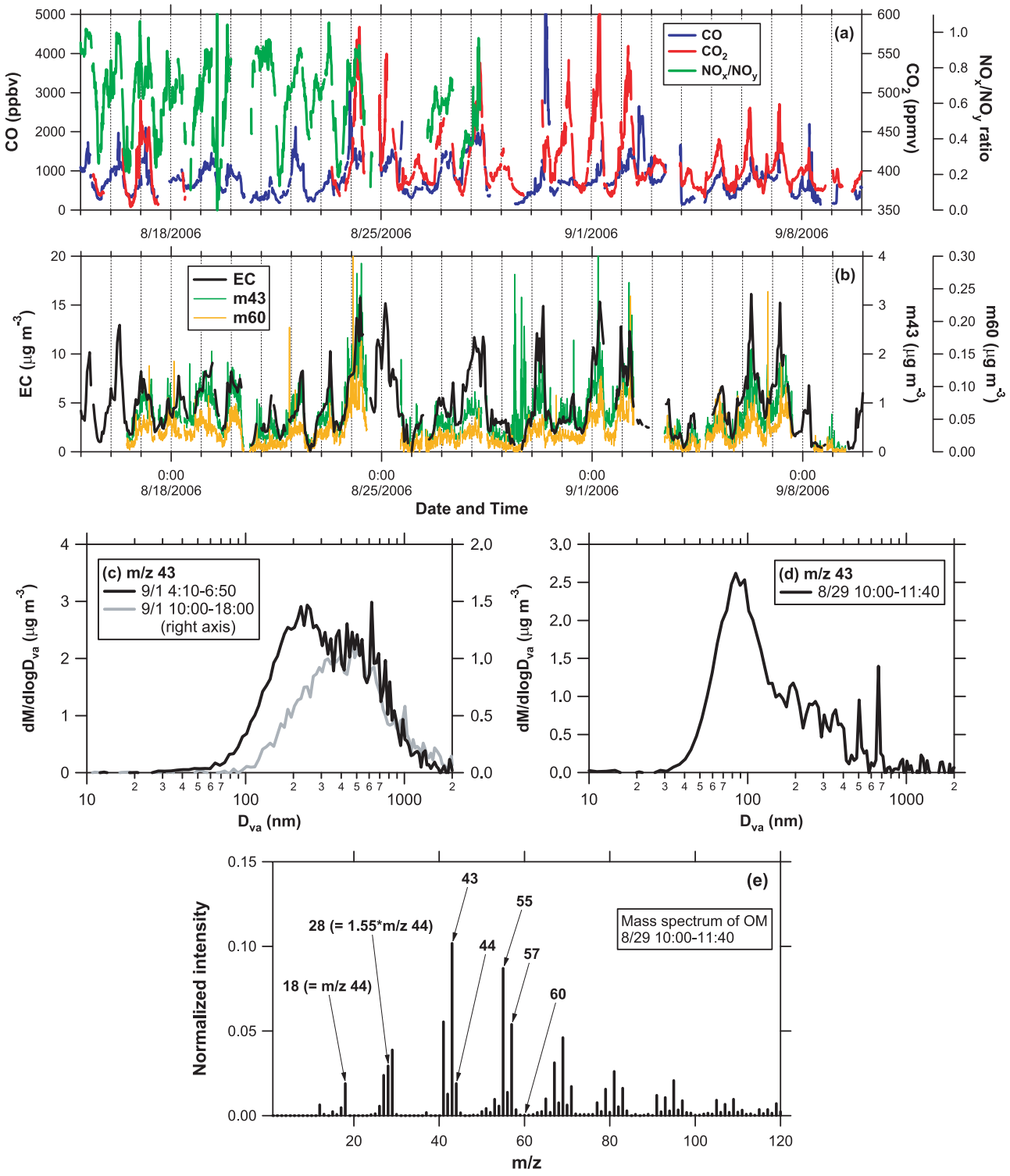

Figure 5. Time series of (a) CO (blue), CO_2 (red), and NO_x/NO_y ratio (green) during the whole measurement period. (b) Time series of EC (black), *m*43 (green), and *m*60 (orange), where *m*43 (or *m*60) is the equivalent mass concentration of organic compounds represented by the signal intensity at *m*/*z* 43 (or *m*/*z* 60) in the AMS mass spectra. (c) Size distributions of *m*43 averaged for 0410–0650 LT (black line) and 1000–1800 LT (shaded line) on 1 September. (d) Same as Figure 5c but for 1000–1140 LT on 29 August. (e) Mass spectrum of OM for 1000–1140 LT on 29 August.

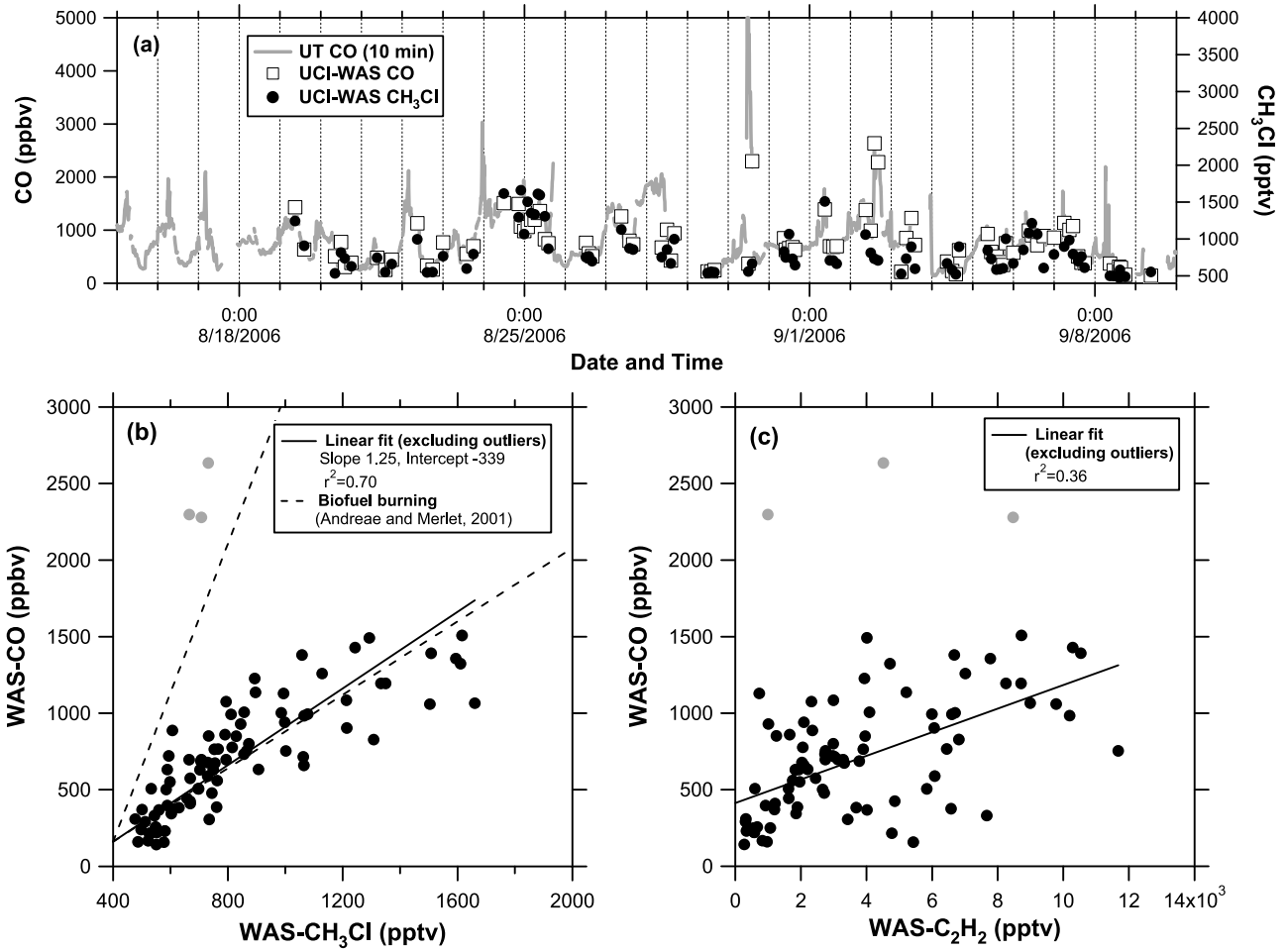

Figure 6. (a) Time series of CO (open squares) and methyl chloride (CH_3Cl: solid squares) measured by whole air sampling (WAS). The online CO data (shaded line) are also plotted for comparison. (b) Correlation of CO versus CH_3Cl measured by WAS. The solid line is the linear regression line, and the dashed lines represent the range of CO/CH_3Cl emission ratios from biofuel burning [*Andreae and Merlet*, 2001]. A few outlying data points (indicated by shaded circles) are excluded from the regression. (c) Same as Figure 6b but for CO versus ethyne (C_2H_2).

these particles also originated from a local source. Figure 5e shows the mass spectrum of organic aerosol corresponding to these spikes. The mass spectrum was normalized so that the sum of all *m*/*z* peaks was equal to unity. It can be characterized by some typical hydrocarbon *m*/*z* peaks (43, 55, 57, etc.) and was similar to those of diesel exhaust particles [e.g., *Canagaratna et al.*, 2004]. However, it is unlikely that these particles originated from combustion sources, considering the absence of correlation with CO, CO_2, and EC. Although the origin of these small particles is unknown at the present stage, this feature was very episodic and would have been a minor source of POA on average.

[39] In summary, the air masses observed during nighttime were significantly affected by local diesel emissions in some cases. This implies that the data obtained during nighttime should be excluded for investigating physical/chemical processing of aerosol on a regional scale.

4.1.2. Influence of Biofuel Burning

[40] Figure 6a shows time series of CO and methyl chloride (CH_3Cl) measured by WAS. The online UT-CO data are also plotted for comparison. The WAS-CO data (~10-s integration time with a ~3-h interval) were simply merged with the UT-CO data (10 min) without any corrections, because the variability of the CO concentration within 10 min was small. The linear regression slope, intercept, and r^2 of WAS-CO versus UT-CO were 0.946, 53 ppbv, and 0.97, respectively, indicating that the agreement between the two independent measurements was as good as their combined accuracies (1.4% for UT-CO and 5% for WAS-CO).

[41] Figures 6b and 6c show the correlations of CO versus CH_3Cl and CO versus ethyne (C_2H_2), respectively, measured by WAS. Excluding a few outlying data points, we have found a tight correlation of CO versus CH_3Cl (r^2 = 0.70) without significant dependence on local time. Note that we used a bivariate regression analysis incorporating the errors in both variables. In general, a positive correlation of pollutants can occur due simply to mixing of polluted air with clean air, even though the emission sources of the pollutants are different. However, the poor correlation of CO versus C_2H_2 (r^2 = 36) (also for CO versus other hydrocarbons, not shown) suggests that the mixing processes alone cannot explain the observed correlation of CO versus CH_3Cl. It has

been shown that biomass/biofuel burning is an important source of CO and CH_3Cl, as summarized by *Andreae and Merlet* [2001]. CH_3Cl is also emitted from charcoal burning, although the emission factor is lower than those from biomass and biofuel burning [*Andreae and Merlet*, 2001]. In the case of this study, open biomass burning is estimated to be a minor source because the Along Track Scanning Radiometer (ATSR) World Fire Atlas detected very few hot spots in the Beijing region during the measurement period (http://dup.esrin.esa.int/ionia/wfa/). On the other hand, biofuel burning in residential sectors, which may not be detected from satellites, could be an important source of pollutants. The slope of CO versus CH_3Cl (1.3 ppbv/pptv) was within the range of CO/CH_3Cl emission ratios that have been measured from biofuel burning [*Andreae and Merlet*, 2001], suggesting that biofuel burning emissions could have been a major source of CO in the observed air masses. On the other hand, the Streets inventory shows that the emissions from domestic sectors were not the dominant source of CO in this region (Table 1), although there are large uncertainties in their estimates. Our results and the Streets inventory are not quantitatively consistent regarding the relative importance of biofuel burning as a source of CO.

[42] As for CO_2, EC, POA, and other compounds, major emission sources affecting the observed concentrations of these species (excluding local diesel emissions during nighttime) have not been identified well from the measurement data. The Streets inventory may give some insights into the relative contribution of each emission category (industry, domestic, etc.) to these species, but they may not be quantitatively consistent with the observations, as we have shown for CO. Evolution of secondary products such as SO_4^{2-} and secondary organic aerosol (SOA) can be investigated using photochemical ages derived from hydrocarbons if locations of major emission sources of aerosols and their precursors are well identified, as performed in previous studies focusing on outflow from typical urban areas [*de Gouw et al.*, 2005; *Takegawa et al.*, 2006a; *Brock et al.*, 2008; *Miyakawa et al.*, 2008]. The complex features of emission sources at the Yufa site make it rather difficult to apply this analysis method.

4.2. Mass Concentrations and Size Distributions of Submicron Aerosol

[43] Figures 7a and 7b show the time series of mass concentration of total measured PM_1 (= EC + OM + SO_4^{2-} + NO_3^- + Cl^- + NH_4^+) and individual species during the whole measurement period. Figures 7c and 7d display time series of the fractional contribution of each component to the total measured PM_1 mass and the SO_4^{2-} size distributions, respectively. Again, we should note that the diameters measured by the AMS represent vacuum aerodynamic diameters under dry conditions. We can see that the total measured PM_1 mass concentrations were highly variable during the measurement period, ranging from ~2 to ~100 $\mu g\ m^{-3}$. Very high and low concentrations of PM_1 mass appeared before and after clean air advection, respectively. The fractional contributions were also variable. Organics were the dominant components at lower PM_1 concentrations, while the contribution of SO_4^{2-} significantly increased during each stagnant period.

[44] A scatterplot of $[NH_4^+]$ versus $2[SO_4^{2-}] + [NO_3^-] + [Cl^-]$ is shown in Figure 8, where [X] denotes the molar concentration of species X. The slope of 0.83 indicates that these anions were mostly, but not fully neutralized by NH_4^+. Note that there may be some uncertainties in the relative ionization efficiency for NH_4^+ (RIE_{NH4}). We used the previously reported, commonly used RIE_{NH4} value of 3.5 as given by *Alfarra et al.* [2004]. Considering that the Berner impactor data also showed slightly lower NH_4^+ than expected (the slope of $[NH_4^+]$ versus [anions] was 0.81), the small deficit in NH_4^+ was unlikely owing to the uncertainty in the RIE_{NH4}. A possible explanation for this phenomenon is some contribution of other cations such as potassium (K^+), Na^+, and Ca^{2+}, and/or the presence of acidic particles. As for the first possibility, the Berner impactor data show that the addition of K^+ increased the cation concentration by ~8% on average (Na^+ and Ca^{2+} were negligible, as described earlier), suggesting that K^+ may have also contributed to the neutralization of the anions. As for the second possibility, NO_3^- and Cl^- needed to have been externally mixed with acidic SO_4^{2-} particles. Figure 9a shows an example of size distributions of SO_4^{2-}, NO_3^-, Cl^-, and NH_4^+ during a stagnant period (1000–1800, 30 August 2006). In the reduction of the NH_4^+ size distributions from AMS particle time-of-flight (P-ToF) data, small corrections were applied to account for the interference of $^{16}O^+$ signals and also for the difference in the ion time of flight in the quadrupole [*Zhang et al.*, 2005b]. Although the Q-AMS cannot quantify the single-particle mixing state in a strict way, the apparently different size distributions of SO_4^{2-} and NO_3^-/Cl^- suggest that some portions of these species were externally mixed in this case. Figure 9b shows the size distributions of molar concentrations of the anions $(2[SO_4^{2-}]) + [NO_3^-] + [Cl^-])$ and NH_4^+ for this case, illustrating the size-dependent ion balance. We can see that the molar concentration of NH_4^+ was slightly lower than anions at $d_{va} < \sim 600$ nm, while they agreed well at $d_{va} > \sim 600$ nm. This result suggests the presence of two dominant modes in the size distributions: a smaller mode (peak at 200–300 nm) consisting mainly of SO_4^{2-} particles that were not fully neutralized and a larger mode (peak at 500–600 nm) consisting mainly of internally and/or externally mixed SO_4^{2-}, NO_3^-, and Cl^- particles that were fully neutralized. Similar results have been found in other cases (not shown). We hypothesize that the possibility of external mixtures of SO_4^{2-}, NO_3^-, and Cl^- particles and dependence of particle acidity on the mixing state could explain the observed phenomena, although this hypothesis has not been validated at this stage.

[45] The size distributions of SO_4^{2-} shown in Figure 7d revealed drastic changes in the mass peak diameter of SO_4^{2-} over the course of a few days, associated with the cycle of stagnant periods and advection of clean air. For example, the peak diameter of SO_4^{2-} continuously increased from ~100 nm on 29 August to ~500 nm on 1 September. Correspondingly, the mass concentration of SO_4^{2-} largely increased from ~4 to ~20 $\mu g\ m^{-3}$ (Figure 7b). A continuous increase in the peak diameter of SO_4^{2-} was also found from 16 to 19 August, although the mass concentration and fractional contribution of each component (including SO_4^{2-} and the others) did not show notable changes. The latter case is interesting because there was a significant change in the physical properties of aerosols without apparent changes in the chemical composition. This case demonstrates the advantage of the AMS measurements because these changes would be captured neither by bulk concentration measurements nor

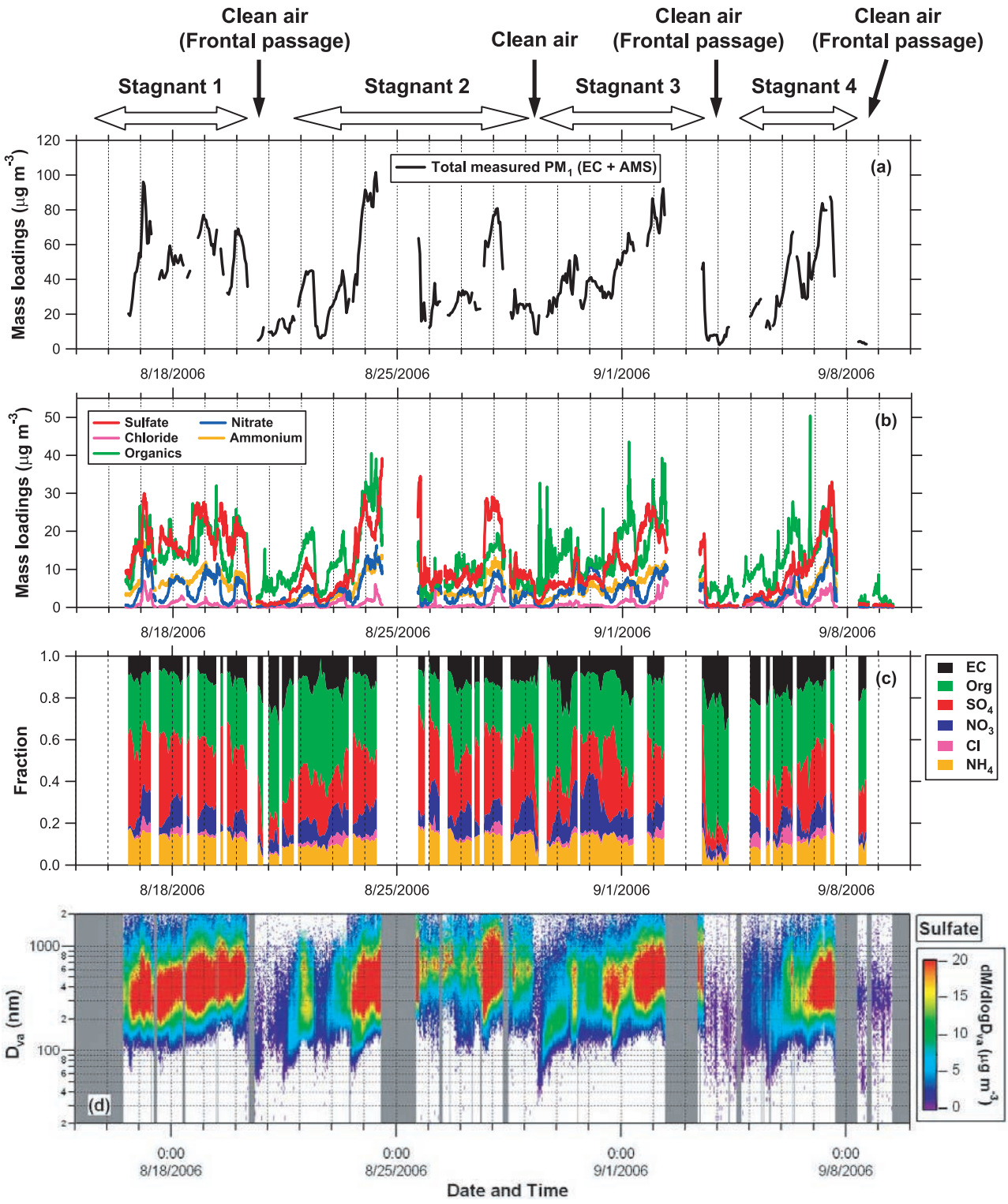

Figure 7. Time series of (a) the mass concentrations of total measured PM_1 aerosol (= EC + OM + SO_4^{2-} + NO_3^- + Cl^- + NH_4^+), (b) individual aerosol species measured by the AMS, and (c) fractional contribution of each component to the total measured PM_1 mass. (d) Image plot of size distribution of SO_4^{2-}. The data were smoothed by running mean (boxcar function, 30-min width). The white areas indicate that the signals were lower than noise levels. The noise level was defined as 2 times the standard deviation of the signals at the particle time-of-flight (P-ToF) range of < 1.5 and > 7 ms, where no particle was expected. The gray areas indicate that data were not obtained.

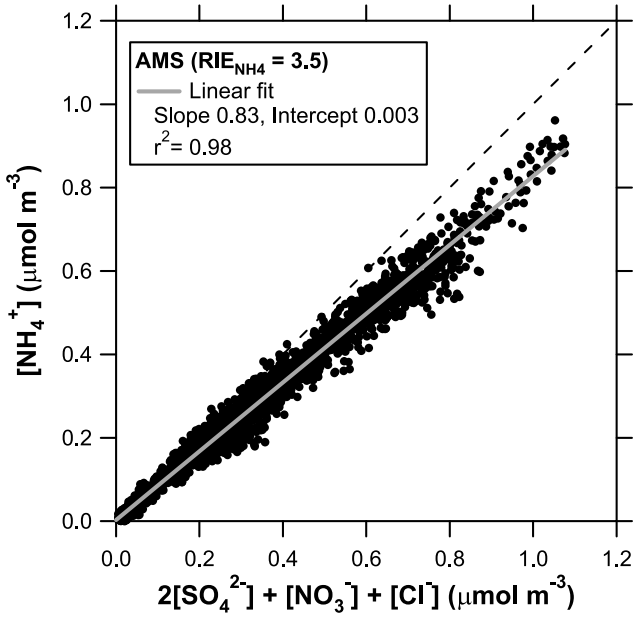

Figure 8. Scatterplot of molar concentrations of $[NH_4^+]$ versus $2[SO_4^{2-}] + [NO_3^-] + [Cl^-]$, where [X] denotes the molar concentration of species X. The shaded line indicates the linear regression line, and the dashed line represents the 1:1 correspondence line.

cascade impactor measurements with relatively coarse sizing and temporal resolution. The large, gradual increases in the mass concentrations and peak diameters on a time scale of a few days during each stagnant period indicate that significant changes in the chemical and physical properties of submicron aerosols occurred on a regional scale rather than a local scale.

[46] It should be noted that growth of Aitken-mode (<100 nm) SO_4^{2-} particles was observed after each clean air event (Figure 7d). Analysis of the aerosol number size distribution indicates that new particle formation events were frequently observed at the Yufa site [*Achtert et al.*, 2009], and the growth of Aitken-mode SO_4^{2-} observed by the AMS was associated with extensive new particle formation events. The ion balance during the particle growth events may be of interest in terms of particle acidity, but is rather difficult to quantify because of low signal-to-noise ratio of NH_4^+ at smaller diameters.

[47] The variability of the SO_4^{2-} size distribution observed at the Yufa site was much more evident than that previously observed at other locations, including Tokyo [*Miyakawa et al.*, 2008], Pittsburgh [*Zhang et al.*, 2005b, 2005c], and Mexico [*Salcedo et al.*, 2006]. In these previous studies, large-mode (~500 nm) SO_4^{2-} particles almost always existed throughout the observation periods, which implies that a significant fraction of the large-mode SO_4^{2-} had been produced outside the cities. In our previous studies in Tokyo, for example, large-mode SO_4^{2-} was predominantly seen even in air masses categorized as fresh urban emissions (NO_x/NO_y ratio <0.2) in summer [*Miyakawa et al.*, 2008]. The unique situation in Beijing is that the contribution of large-mode SO_4^{2-} transported from other areas was much smaller than that produced in this region during air mass stagnation.

4.3. Temporal Variations of SO_4^{2-}, *m/z* 44, and O_3

[48] Time series of mass concentrations of SO_4^{2-} and *m*44 are shown in Figure 10a. *m/z* 44 (CO_2^+) is a good marker of particle-phase carboxylic acids [e.g., *Alfarra*, 2004; *Takegawa et al.*, 2007]. *m/z* 44 has been identified as one of the major peaks in the mass spectra of SOA compounds in smog chamber studies [e.g., *Bahreini et al.*, 2005], although the chamber results should be interpreted with caution because the mass spectrum pattern can significantly vary depending on mass loading [*Shilling et al.*, 2008]. The temporal variation of *m*44 was very similar to that of SO_4^{2-} at the Yufa site. The time series did not show distinct diurnal variations but showed day-to-day variations associated with the cycle of stagnant periods and advection of clean air.

[49] Figure 10b shows temporal variations of the mass peak diameter of SO_4^{2-} and *m/z* 44 derived from 2-h average size distributions. We did not apply lognormal fitting but simply selected the peak diameter at $d_{va} < 1$ μm. The derived peak diameter may not have been statistically meaningful when its peak height was comparable to the height of the noise signals. In the AMS P-ToF data, no particle was expected to have been in the P-ToF range of >7 ms. We use the result only when the derived peak height exceeded three times the maximum noise height in the no-particle region. We can see that the hourly variations of the peak diameters of SO_4^{2-} and *m/z* 44 tracked fairly well: the linear regression slope of *m/z* 44 versus SO_4^{2-} peaks was 0.95 ($r^2 = 0.52$) when forced through the origin.

[50] Similarity in the temporal variations of mass concentrations and size distributions of SO_4^{2-} and *m*44 (or oxygenated organic aerosol: OOA) has been observed in other

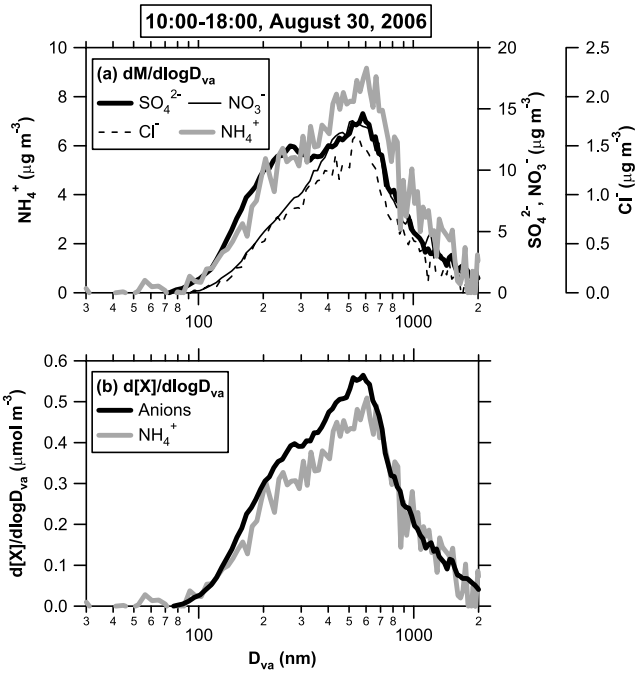

Figure 9. (a) Size distributions of SO_4^{2-} (thick line) NO_3^- (thin line), Cl^- (dashed line), and NH_4^+ (shaded line) during stagnant period (1000–1800 LT, 30 August 2006). (b) Same as Figure 9a but for molar concentrations of the anions (black line) and NH_4^+ (shaded line).

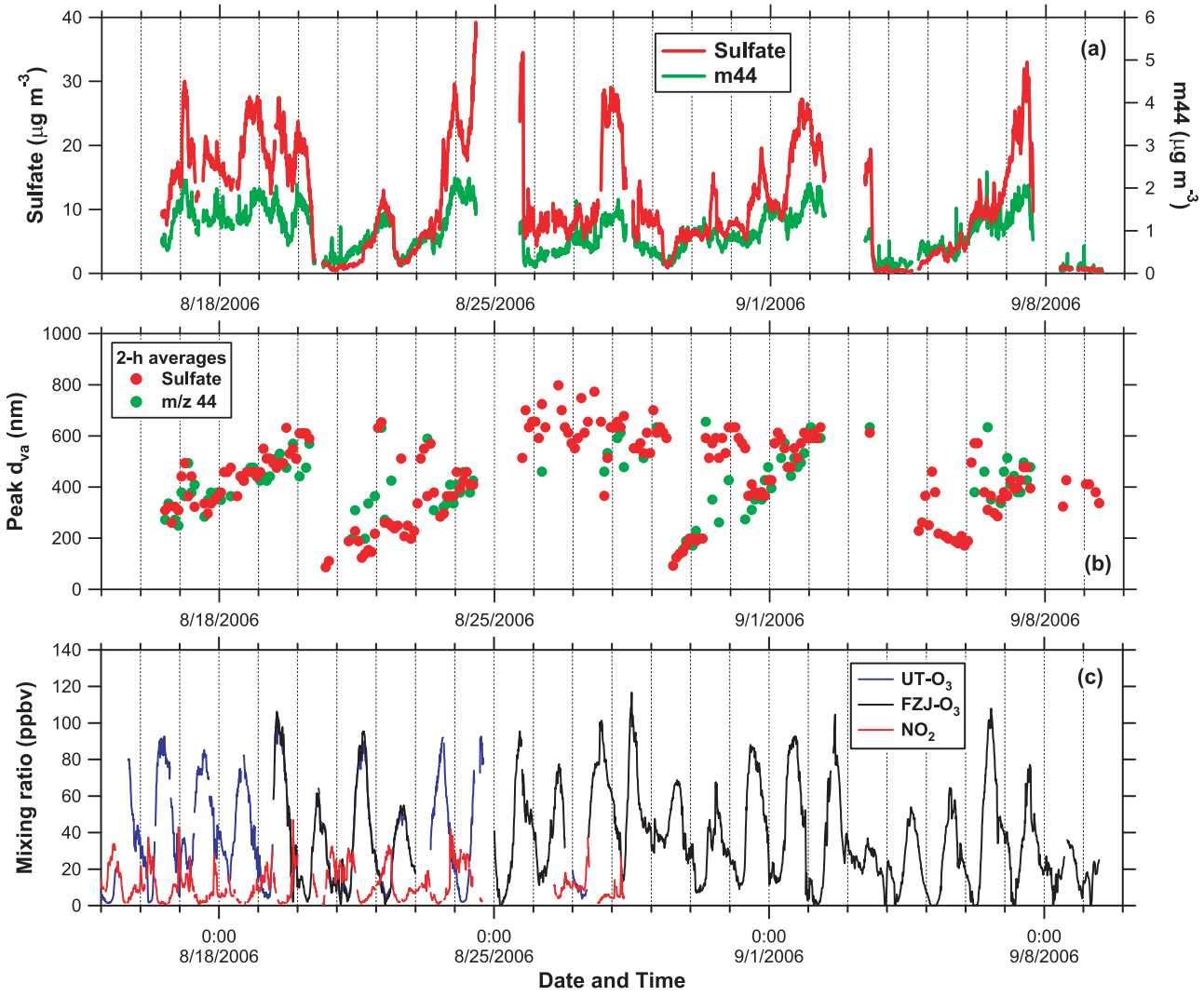

Figure 10. Time series of (a) mass concentrations of SO_4^{2-} (red) and *m*44 (green), (b) peak diameters of SO_4^{2-} (red) and *m*44 (green), and (c) mixing ratios of UT-O_3 (blue), FZJ-O_3 (black), and NO_2 (red).

locations, including Pittsburgh [*Zhang et al.*, 2005c] and Switzerland [*Lanz et al.*, 2007]. It would be of great interest to investigate whether there could be a common mechanism to explain the similarity between SO_4^{2-} and *m*44 at various locations.

[51] Time series of the mixing ratios of O_3 and NO_2 are shown in Figure 10c. Ozone exhibited distinct diurnal cycles, resulting in poor correlations of SO_4^{2-} and *m*44 versus O_3. Although the daytime peaks of O_3 tended to be higher with increasing SO_4^{2-} and *m*44 in some cases, no systematic correlation was identified. This feature does not significantly change even when we use odd oxygen ($O_x = O_3 + NO_2$) instead of O_3, as shown in Figure 10c. By contrast, we found a tight correlation of *m*44 (or OOA) versus O_3 in Tokyo and its outflow region in summer [*Takegawa et al.*, 2006a, 2006b; *Kondo et al.*, 2008]. One of the major differences between the Yufa and Tokyo cases is the residence time of air masses. The photochemical age of the air masses observed in Tokyo and its outflow region in summer was less than 1 day [*Takegawa et al.*, 2006a; *Miyakawa et al.*, 2008], which was much shorter than the duration of each stagnant period in Yufa. In general, removal of submicron aerosol by dry deposition is considerably slower than that of O_3 [*Lovett*, 1994]. The fraction of SOA carried over from previous days could be much larger than that of O_3 with increasing the residence time of air masses. In fact, daily minimum concentrations of *m*44 observed at the Yufa site tended to be higher as air mass stagnation proceeded. This effect was likely the major cause of the poor correlation of *m*44 versus O_3 in Yufa.

4.4. Importance of SO_4^{2-} at Higher Mass Loadings

[52] Figure 11 shows the ratio of OM to total measured PM_1 mass (OM fraction) as a function of total measured PM_1 mass. The data were classified according to local time and color-coded by SO_4^{2-} fraction. This plot is conceptually the same as that presented by *Brock et al.* [2008]. The only difference is that *Brock et al.* [2008] used total sulfur (SO_2 + SO_4^{2-}) or sulfate mass as a parameter for color-coding and we used SO_4^{2-} fraction. Figure 11 indicates the dominance of OM at lower total PM_1 mass loadings and that of SO_4^{2-} at higher mass loading. This tendency is more evident during the daytime than nighttime. This is likely because additional

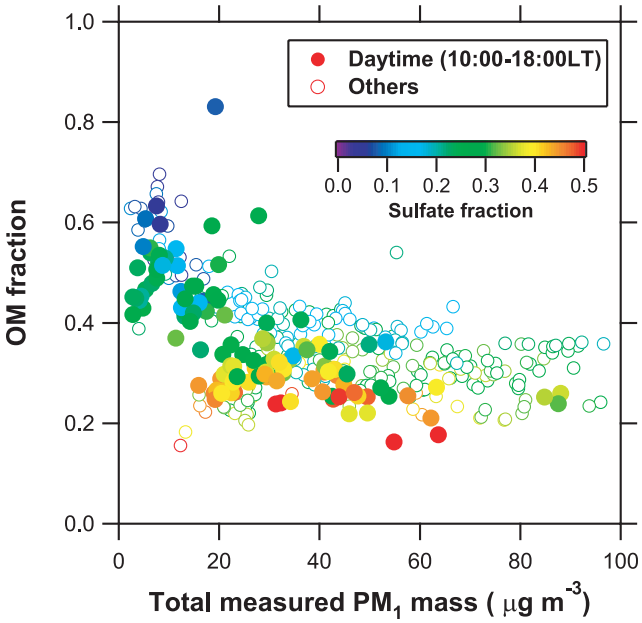

Figure 11. Ratio of OM to total measured PM_1 mass (OM fraction) as a function of total measured PM_1 mass. Solid circles represent the data obtained during the daytime (1000–1800 LT) and open circles represent those from evening to the following morning (1800–1000 LT). The data points are color-coded by SO_4^{2-} fraction.

injection of OM from local sources enhanced PM_1 mass loadings during the nighttime. Although this feature is also inferred from Figure 7 as stated in section 4.2, it can be more clearly illustrated by Figure 11. The dependence of PM_1 mass on SO_4^{2-} and OM fractions is quantitatively similar to that obtained by *Brock et al.* [2008].

[53] Our result may have an important implication for the PM control strategy in Beijing. The dominance of SO_4^{2-} at higher total PM_1 mass loadings implies that reduction of SO_2 should lead to significant reduction of PM in Beijing. Large point sources such as power plants are the major sources of SO_2 in this region [*Streets et al.*, 2003], and the reduction of SO_2 from such point sources would be more cost-effective and realistic than reduction of POA and VOCs whose emission sources are highly uncertain and spread over wide areas.

5. Estimates of Regional-Scale Processing

[54] Here we focus on the evolution of SO_4^{2-} during stagnation periods, with some relations to *m*44. Evolution of SOA (and NO_3^-) would also be important in order to investigate the changes in overall aerosol composition with air mass stagnation. However, separation of POA/SOA and estimate of SOA forming potentials from various precursor VOCs require significant additional analysis, which is beyond the scope of this paper.

5.1. Assumption

[55] As we described in sections 3.2 and 4.1, the air masses observed during the nighttime were likely affected by local emission sources. Conversely, the data obtained during the daytime (1000–1800 LT) may have been less affected by local sources than the nighttime data because of higher wind speeds and ML heights. Here we assume that the data obtained during the daytime (1000–1800 LT) can be used for investigating the characteristics of aerosol on a regional scale. The trajectory analysis in section 3.1 indicates that air masses were generally confined to within ~500 km distance from the site during the preceding 2 days in each stagnant period. Therefore, the term "regional scale" in this study represents a few hundred km.

5.2. Evolution of Mass Concentrations

[56] Figure 12 displays daytime averages (1000–1800 LT) of EC and SO_4^{2-} mass concentrations during each stagnant period. A time series of SO_2 mixing ratios is also shown. Regression slopes of the daytime average values for each stagnant period can be regarded as increasing rates of these species by regional-scale processing. Note that the regression analysis was not meaningful for stagnant period 2 (22–28 August) because the aerosol concentrations rapidly changed after the temporal gap of the AMS data between 24–25 August. The change in the aerosol concentrations may be due to the rainfall event in the midnight of 25 August (Figure 4b). The uncertainties in the slopes were evaluated by varying the time window for the daytime average (1000–1600 LT and 1200–1800 LT), as shown in Table 2. The estimated uncertainties were found to be comparable to the errors (1-σ) due to the linear regression fit (as shown in the legend of Figure 12).

[57] Elemental carbon can be used to estimate effects of dilution/mixing on SO_2 because the locations of major emission sources of EC and SO_2 are similar on a regional scale (Figure 2). Carbon monoxide and CO_2 could also be used for this purpose. Here we use EC for the present analysis because temporal coverage of EC was better than that of CO and CO_2. EC showed an increasing trend during stagnant period 1, but there were no significant trends during periods 3 and 4. Increasing/decreasing trends of EC can be used as diagnostics for the relative contributions from additional emissions and dilution during air mass stagnation. No decreasing trend of EC during stagnant periods 1, 3, and 4 is interpreted as an additional injection of EC during air mass stagnation compensating for a possible decrease in EC by dilution. This interpretation could also be applicable to SO_2.

[58] Sulfate showed increasing trends during stagnant periods 1, 3, and 4, ranging from 3.8 to 8.2 $\mu g\ m^{-3}\ d^{-1}$. The large increasing rates of SO_4^{2-} during stagnant periods 3 and 4 indicate that secondary formation of SO_4^{2-} significantly exceeded a possible decrease in SO_4^{2-} either by dilution or dry/wet deposition during these periods. Note that the increasing rates of SO_4^{2-} estimated by the regression analysis should be regarded as the lower limits of the overall production rates of SO_4^{2-} (including both gas-phase and aqueous-phase reactions) considering possible decrease in SO_4^{2-} by dilution and/or deposition.

5.3. Evolution of Size Distributions

[59] Figure 13 displays the daytime (1000–1800 LT) averaged size distributions of SO_4^{2-} and *m*44 during stagnant periods 1, 3, and 4. Significant, gradual shifts of SO_4^{2-} size distributions during each stagnant period can be clearly identified. The size distributions of *m*44 showed a shape very similar to those of SO_4^{2-} for the duration of this time period.

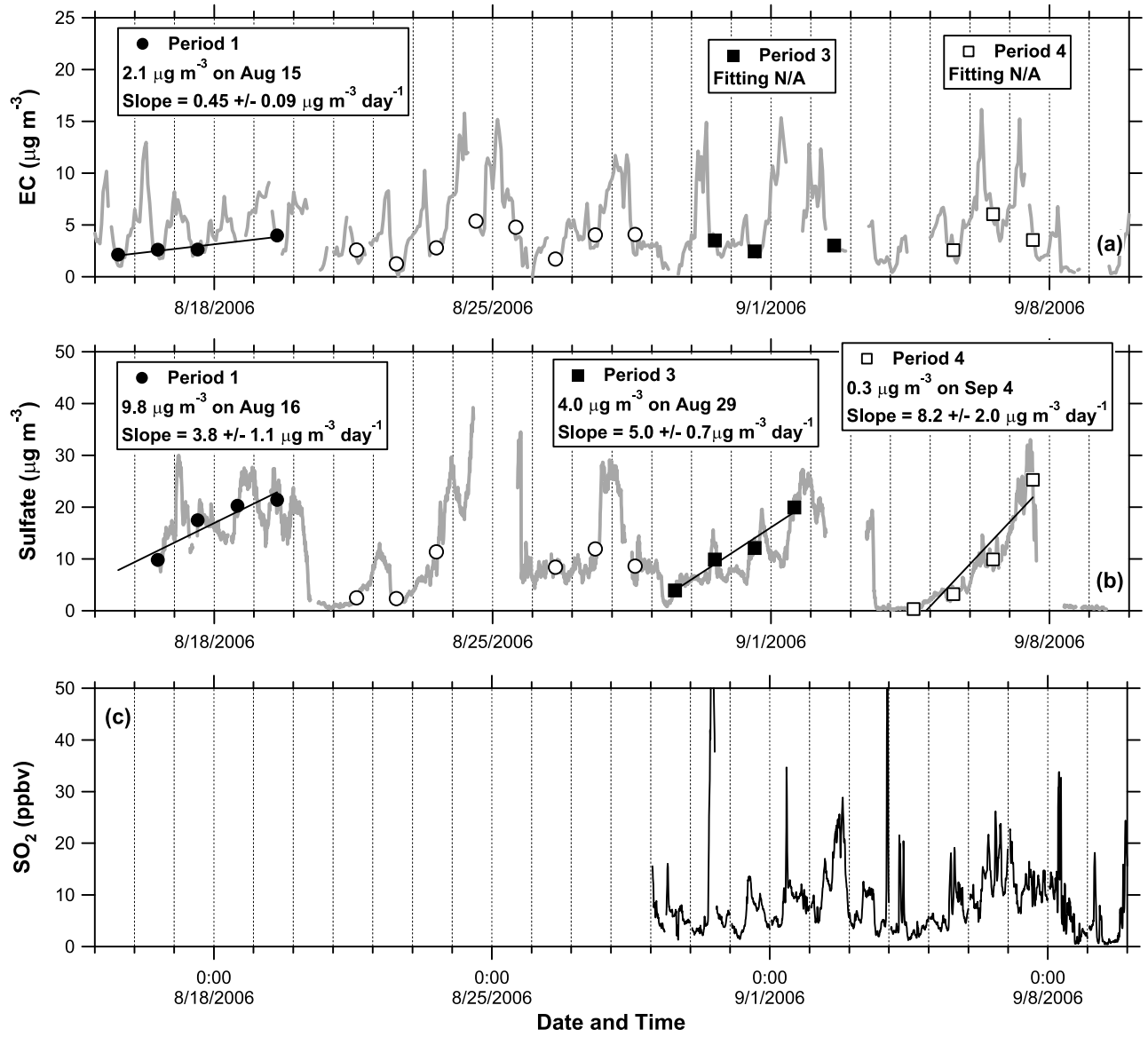

Figure 12. Daytime averages (1000–1800 LT) of (a) EC and (b) SO_4^{2-} during stagnant period 1 (solid circles), period 2 (open circles), period 3 (solid squares), and period 4 (open squares). A linear regression was calculated for each stagnant period. (c) Time series of SO_2 mixing ratios.

Table 2. Comparison of the Observed Increasing Rate and Estimated Gas-Phase Production Rate of SO_4^{2-} (at 25°C and 1 atm) for Each Period

	Averages for Each Period			
	Period 1 (15–19 Aug)	Period 2 (22–28 Aug)	Period 3 (29 Aug to 2 Sep)	Period 4 (4–7 Sep)
OH[a] (molec cm^{-3})	4.2×10^6	2.9×10^6	2.8×10^6	2.1×10^6
Lifetime of SO_2 (days)	2.8	4.1	4.2	5.6
SO_2 (ppbv)	N/A	N/A	9.6	9.1
Gas-phase production rate of SO_4^{2-}[b] ($\mu g\ m^{-3}\ d^{-1}$)	N/A	N/A	9.0	6.4
Increasing rate of SO_4^{2-}[c] ($\mu g\ m^{-3}\ d^{-1}$)	3.8 (4.4, 3.6)	N/A	5.0 (4.8, 5.2)	8.2 (8.3, 9.8)

[a]Diurnally averaged OH concentrations from the LIF measurements were used.
[b]We assume that all of the SO_2 oxidized by OH reaction was converted to SO_4^{2-}.
[c]Values in parentheses are the estimates when varying the time window for the daytime average (1000–1600 LT and 1200–1800 LT, respectively).

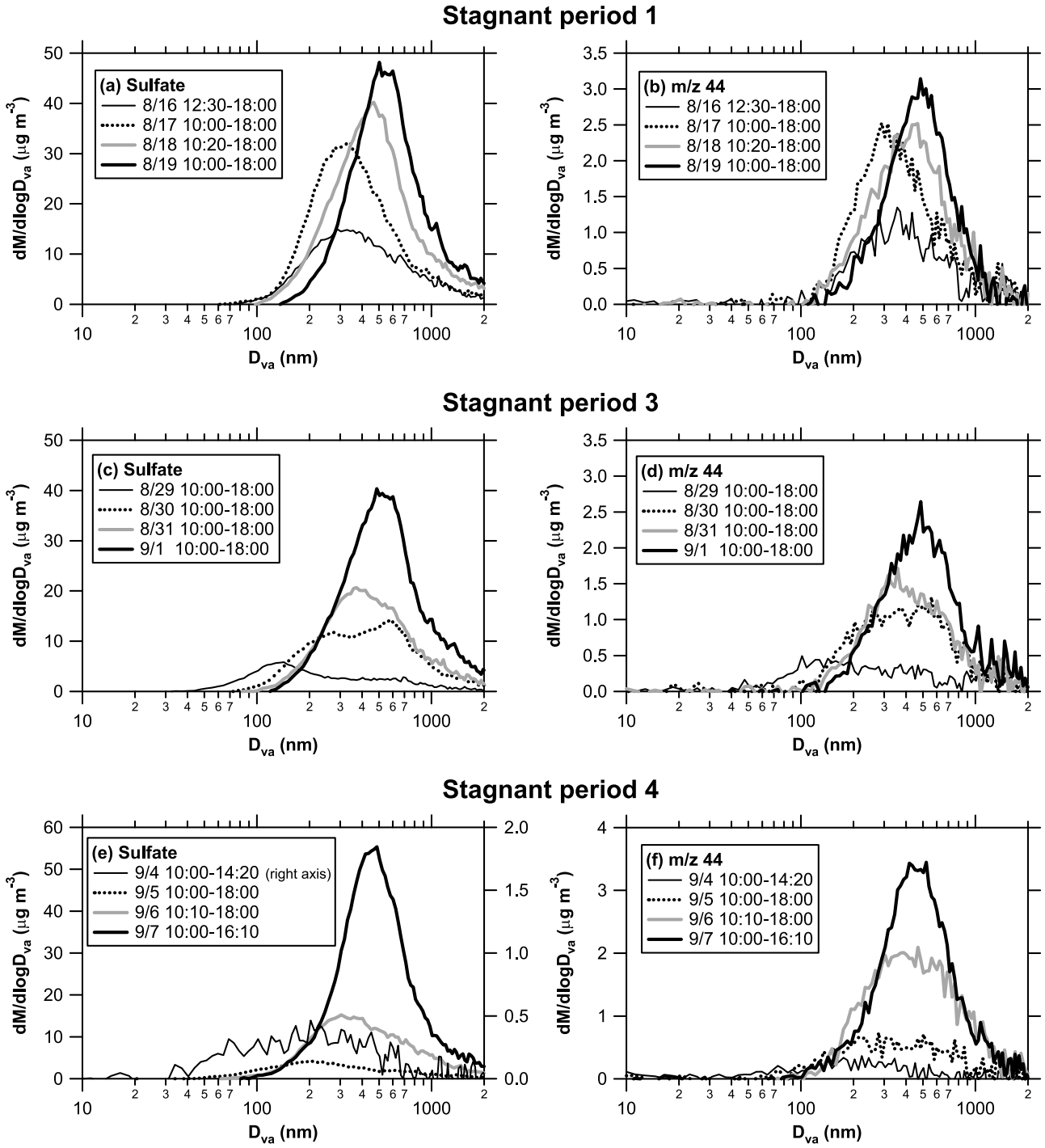

Figure 13. Day-to-day series of average size distribution of SO_4^{2-} and *m*44 in daytime (1000–1800 LT) during stagnant periods 1, 3, and 4.

Although the correlation of the peak diameters of SO_4^{2-} and *m*44 has already been described in section 4.3 (Figure 10), the similarity in the size distributions can be more clearly illustrated by Figure 13. The growth of SO_4^{2-} observed during stagnant period 3 was slightly different from that during the other periods. The SO_4^{2-} size distributions on 29, 30, and 31 August showed bimodal peaks. The peak diameter of the small mode was ~135 nm on 29 August and finally merged into the large mode at ~540 nm on 1 September. On the other hand, the SO_4^{2-} size distributions during stagnant periods 1 and 4 can be approximated as monomodal over the course of a few days. We should note that the peak diameters and mass concentrations observed on 19 August and 1 September may have been slightly underestimated because the transmission efficiency of the aerodynamic lens is reduced at $d_{va} > 600$ nm [*Jayne et al.*, 2000; *Takegawa et al.*, 2009].

Nevertheless, the observations clearly indicated that the peak diameter of SO_4^{2-} increased gradually from d_{va} ~100 nm to d_{va} ~500 nm over the course of a few days.

6. Discussion

[60] First, we investigate whether the increasing rates of SO_4^{2-} bulk mass concentration inferred from the observations can be explained by gas-phase oxidation of SO_2. Table 2 summarizes some parameters of SO_2 and OH during each period (including both daytime and nighttime). The photochemical lifetime of SO_2 due to OH reaction for each stagnant period was estimated using the diurnally averaged OH concentration based on the LIF measurements and assuming constant temperature and pressure (25°C and 1 atm). The gas-phase production rate of SO_4^{2-} is simply a conversion of units from the SO_2 oxidation rate at 25°C and 1 atm.

[61] We should note that there could be substantial uncertainties in the estimated gas-phase production rate of SO_4^{2-} due to the assumption of a constant SO_2 concentration. The SO_2 mass concentrations in the upper part of the ML were likely lower than those at the surface (i.e., inhomogeneous in vertical), resulting in possible overestimation of the average production rates in the ML. On the other hand, the SO_2 concentrations near the emission sources would be higher than those observed at the Yufa site (i.e., effects of dilution and/or removal of SO_2), resulting in possible underestimation of the production rate over the course of the air mass histories.

[62] As described in section 5.2, the increasing rates of SO_4^{2-} determined by the regression analysis could also underestimate the overall production rates of SO_4^{2-} in this region owing to possible decrease in SO_4^{2-} by dilution and/or deposition. Although there are substantial uncertainties in both the production rates of SO_4^{2-} estimated from the SO_2 + OH reaction and the increasing rates of SO_4^{2-} determined by the regression analysis, our best estimates suggest that these two numbers were comparable for stagnant periods 3 and 4, and that gas-phase oxidation of SO_2 can potentially explain the formation of SO_4^{2-} to a large extent during these periods. However, this does not necessarily mean that gas-phase reaction can explain the observed increase in the diameter of SO_4^{2-}, as discussed by *Meng and Seinfeld* [1994].

[63] Previous studies identified two distinct modes in mass size distributions of submicron SO_4^{2-} in urban air [e.g., *Hering and Friedlander*, 1982]. The smaller mode is the condensation mode (200 ± 100 nm aerodynamic diameter) and the larger one is the droplet mode (700 ± 200 nm). The presence of the droplet mode cannot be explained by growth of the condensation mode through gas-phase oxidation, and is instead attributed to cloud processing [*Meng and Seinfeld*, 1994]. *Kerminen and Wexler* [1995] investigated the characteristic time of SO_4^{2-} growth from the condensation mode to droplet mode for the South Coast Air Basin of Los Angeles (SoCAB) and concluded that only aqueous-phase oxidation was sufficiently fast to explain the particle growth on a reasonable time scale (<1 day) for the SoCAB case.

[64] In this study we have found that the peak diameter of SO_4^{2-} increased gradually from d_{va} ~ 100 nm to d_{va} ~ 500 nm over the course of a few days. The diameter of d_{va} ~ 500 nm was comparable to the droplet mode diameter observed during the SoCAB. Considering the high concentrations of precursors and frequent appearances of low-level clouds during the measurement period (Figure 4), aqueous-phase oxidation could have been sufficiently fast to explain the observed particle growth. However, the fraction of time when the observed air masses encountered clouds is highly uncertain. The rate of SO_4^{2-} formation by aqueous-phase reaction depends on the diameter and pH of cloud droplets and the concentrations of other oxidants such as hydrogen peroxide (H_2O_2) and O_3 [*Kerminen and Wexler*, 1995, and references therein], which are also highly uncertain in this case (except for O_3). Without information on these important factors, it is not realistic to estimate the contribution of aqueous-phase reaction to the particle growth in this study.

[65] The above discussion is not precise enough to draw definitive conclusions on the relative importance of condensation and aqueous-phase reaction regarding the formation of SO_4^{2-} in this region. An addition of aqueous-phase reaction may significantly overestimate the overall production rate of SO_4^{2-} if the contribution of aqueous-phase reaction was comparable to or larger than that of gas-phase reaction (Table 2). An alternative approach may be the so-called growth law analysis based on temporal changes in number size distribution [e.g., *McMurry and Wilson*, 1982]. This analysis technique is generally applicable to Lagrangian plumes with negligible contributions from additional primary emission and coagulation, which is not the case in this study. Further studies using three-dimensional models incorporating size-resolved aerosol schemes (e.g., sectional approaches) are needed to investigate and quantify the controlling factors affecting the particle formation and growth in this region.

7. Summary

[66] AMS data obtained at a rural site in Beijing in the summer of 2006 were used to investigate the variability of chemical composition and size distribution of submicron aerosol in this region. On the basis of backward trajectories and surface meteorological data, the measurement period was characterized by the cycle of stagnant periods and rapid advection of clean air. The advection of clean air was mostly due to the passage of a midlatitude cyclone associated with a cold front. This synoptic-scale meteorology was found to be an important factor affecting the variability of the aerosol concentrations.

[67] The temporal variations of CO, CO_2, EC, and other combustion tracers indicated that the types of emission sources around the measurement site were highly variable and complex, depending on local time. It is likely that the air masses observed during nighttime were significantly affected by local diesel emissions. The tight correlation of CO versus CH_3Cl suggested that biofuel burning was a major source of CO. On the other hand, major emission sources of CO_2, EC, POA, and other compounds have not been well identified from the measurement data.

[68] The mass concentration of total measured PM_1 (= EC + OM + SO_4^{2-} + NO_3^- + Cl^- + NH_4^+) showed large variability (from ~2 to ~100 $\mu g\ m^{-3}$) associated with the cycle of stagnant periods and advection of clean air. The size distribution of SO_4^{2-} showed drastic changes over the course of a few days, associated with the meteorological cycle. The temporal variations of SO_4^{2-} and $m44$ (a good marker of SOA) were very similar both in terms of mass concentration and size distribution. These results indicate that both

chemical and physical properties of aerosols were significantly altered owing to secondary formation of aerosol on a regional scale.

[69] We found the dominance of OM at lower total PM_1 mass loadings and that of SO_4^{2-} at higher mass loading. The dependence of PM_1 mass on SO_4^{2-} and OM fractions was quantitatively similar to that obtained by *Brock et al.* [2008]. Our result may have an important implication for the PM control strategy in Beijing. The reduction of SO_2 should lead to significant reduction of PM in this region. This would be more cost-effective and realistic than reduction of POA and VOCs whose emission sources are highly uncertain and spread over wide areas.

[70] The data obtained in daytime (1000–1800 LT) during stagnant periods were used to investigate regional-scale processing (a few hundred kilometers) and its controlling factors. We found systematic increases in the mass concentration and peak diameter of SO_4^{2-} during each stagnant period. The increasing rates of SO_4^{2-} mass concentrations were estimated to be 3.8–8.2 $\mu g\ m^{-3}\ d^{-1}$, which were comparable to the production rates of SO_4^{2-} by gas-phase reaction of SO_2 + OH. The peak diameter of SO_4^{2-} increased gradually from $d_{va} \sim 100$ nm to $d_{va} \sim 500$ nm over the course of a few days. The relative contributions of condensation and aqueous-phase reactions to the particle growth are not clear at the present stage.

[71] This study suggests that significant physical/chemical processing took place on a regional scale during the stagnation of air masses over Beijing. It would be interesting and challenging to simulate the evolutions of mass concentration and size distribution of SO_4^{2-} (and SOA) that are simultaneously occurring in this region.

[72] **Acknowledgments.** The authors acknowledge the NOAA Air Resources Laboratory (ARL) for providing the HYSPLIT transport and dispersion model and READY website (http://www.arl.noaa.gov/ready.html) used in this publication. The measurements by the UT group were supported by the Japan Society for the Promotion of Science (JSPS). This measurement campaign was conducted as a part of CAREBEIJING 2006, which was supported by Beijing Council of Science and Technology (HB200504–6, HB200504–2). This study was conducted also as a part of the Mega-Cities: Asia Task under the framework of the International Global Atmospheric Chemistry (IGAC) project.

References

Achtert, P., W. Birmili, A. Nowak, B. Wehner, A. Wiedensohler, N. Takegawa, Y. Kondo, Y. Miyazaki, M. Hu, and T. Zhu (2009), Hygroscopic growth of tropospheric particle number size distributions over the North China Plain, *J. Geophys. Res.*, doi:10.1029/2008JD010921, in press.

Alfarra, M. R. (2004), Insights into atmospheric organic aerosols using an aerosol mass spectrometer, Ph.D. thesis, Univ. of Manchester, Manchester, U. K.

Alfarra, M. R., et al. (2004), Characteristics of urban and rural organic particulate in the Lower Fraser Valley using two Aerodyne aerosol mass spectrometers, *Atmos. Environ.*, *38*, 5745–5758, doi:10.1016/j.atmosenv.2004.01.054.

Alfarra, M. R., A. S. H. Prevot, S. Szidat, J. Sandradewi, S. Weimer, V. Lanz, D. Schreiber, M. Mohr, and U. Baltensperger (2007), Identification of the mass spectral signature of organic aerosols from wood burning emissions, *Environ. Sci. Technol.*, *41*, 5770–5777, doi:10.1021/es062289b.

Allan, J. D., et al. (2003), Quantitative sampling using an Aerodyne aerosol mass spectrometer: 2. Measurements of fine particulate chemical composition in two U.K. cities, *J. Geophys. Res.*, *108*(D3), 4091, doi:10.1029/2002JD002359.

Allan, J. D., et al. (2004), Submicron aerosol composition at Trinidad Head, California, during ITCT 2K2: Its relationship with gas phase volatile organic carbon and assessment of instrument performance, *J. Geophys. Res.*, *109*, D23S24, doi:10.1029/2003JD004208.

Andreae, M. O., and P. Merlet (2001), Emissions of trace gases and aerosols from biomass burning, *Global Biogeochem. Cycles*, *15*, 955–966, doi:10.1029/2000GB001382.

Bahreini, R., M. D. Keywood, N. L. Ng, V. Varutbangkul, S. Gao, R. C. Flagan, J. H. Seinfeld, D. R. Worsnop, and J. L. Jimenez (2005), Measurement of secondary organic aerosol from oxidation of cycloalkenes, terpenes, and *m*-xylene using an Aerodyne aerosol mass spectrometer, *Environ. Sci. Technol.*, *39*, 5674–5688, doi:10.1021/es048061a.

Bellouin, N., O. Boucher, J. Haywood, and M. S. Reddy (2005), Global estimate of aerosol direct radiative forcing from satellite measurements, *Nature*, *438*, 1138–1141, doi:10.1038/nature04348.

Birch, M. E., and R. A. Cary (1996), Elemental carbon-based method for monitoring occupational exposures to particulate diesel exhaust, *Aerosol Sci. Technol.*, *25*, 221–241.

Brock, C. A., et al. (2008), Sources of particulate matter in the northeastern United States in summer: 2. Evolution of chemical and microphysical properties, *J. Geophys. Res.*, *113*, D08302, doi:10.1029/2007JD009241.

Canagaratna, M. R., et al. (2004), Chase studies of particulate emissions from in-use New York City vehicles, *Aerosol Sci. Technol.*, *38*, 555–573.

Charlson, R. J., S. E. Schwartz, J. M. Hales, R. D. Cess, J. A. Coakley Jr., J. E. Hansen, and D. J. Hofmann (1992), Climate forcing by anthropogenic aerosols, *Science*, *255*, 423–430, doi:10.1126/science.255.5043.423.

Chung, S. H., and J. H. Seinfeld (2002), Global distribution and climate forcing of carbonaceous aerosols, *J. Geophys. Res.*, *107*(D19), 4407, doi:10.1029/2001JD001397.

DeCarlo, P., J. G. Slowik, D. R. Worsnop, P. Davidovits, and J. L. Jimenez (2004), Particle morphology and density characterization by combined mobility and aerodynamic diameter measurements. Part 1: Theory, *Aerosol Sci. Technol.*, *38*, 1185–1205, doi:10.1080/027868290903907.

de Gouw, J. A., et al. (2005), Budget of organic carbon in a polluted atmosphere: Results from the New England Air Quality Study in 2002, *J. Geophys. Res.*, *110*, D16305, doi:10.1029/2004JD005623.

Dockery, D. W., C. A. Pope, X. Xu, J. D. Spengler, J. H. Ware, M. E. Fay, B. G. Ferris, and F. E. Speizer (1993), An association between air pollution and mortality in six US cities, *N. Engl. J. Med.*, *329*, 1753–1759, doi:10.1056/NEJM199312093292401.

Duan, F. K., X. D. Liu, T. Yu, and H. Cachier (2004), Identification and estimate of biomass burning contribution to the urban aerosol organic carbon concentrations in Beijing, *Atmos. Environ.*, *38*, 1275–1282, doi:10.1016/j.atmosenv.2003.11.037.

Duan, F. K., K. B. He, Y. L. Ma, F. M. Yang, X. C. Yu, S. H. Cadle, T. Chan, and P. A. Mulawa (2006), Concentration and chemical characteristics of PM2.5 in Beijing China: 2001–2002, *Sci. Total Environ.*, *355*, 264–275, doi:10.1016/j.scitotenv.2005.03.001.

Guinot, B., H. Cachier, J. Sciare, Y. Tong, W. Xin, and Y. Jianhua (2007), Beijing aerosol: Atmospheric interactions and new trends, *J. Geophys. Res.*, *112*, D14314, doi:10.1029/2006JD008195.

Hering, S. V., and S. K. Friedlander (1982), Origins of aerosol sulfur size distributions in the Los Angeles Basin, *Atmos. Environ.*, *16*, 2647–2656, doi:10.1016/0004-6981(82)90346-8.

Hinds, W. C. (1999), *Aerosol Technology*, John Wiley, Hoboken, N. J.

Holland, F., A. Hofzumahaus, J. Schäfer, A. Kraus, and H.-W. Pätz (2003), Measurements of OH and HO_2 radical concentrations and photolysis frequencies during BERLIOZ, *J. Geophys. Res.*, *108*(D4), 8246, doi:10.1029/2001JD001393.

Jayne, J. T., D. C. Leard, X. F. Zhang, P. Davidovits, K. A. Smith, C. E. Kolb, and D. R. Worsnop (2000), Development of an aerosol mass spectrometer for size and composition analysis of submicron particles, *Aerosol Sci. Technol.*, *33*(1–2), 49–70, doi:10.1080/027868200410840.

Kerminen, V. M., and A. S. Wexler (1995), Growth laws for atmospheric aerosol particles: An examination of the bimodality of the accumulation mode, *Atmos. Environ.*, *29*, 3263–3275, doi:10.1016/1352-2310(95)00249-X.

Kondo, Y., et al. (2006), Temporal variations of elemental carbon in Tokyo, *J. Geophys. Res.*, *111*, D12205, doi:10.1029/2005JD006257.

Kondo, Y., et al. (2008), Formation and transport of oxidized reactive nitrogen, ozone, and secondary organic aerosol in Tokyo, *J. Geophys. Res.*, *113*, D21310, doi:10.1029/2008JD010134.

Lanz, V. A., M. R. Alfarra, U. Baltensperger, B. Buchmann, C. Hueglin, and S. H. Prévôt (2007), Source apportionment of submicron organic aerosols at an urban site by factor analytical modelling of aerosols mass spectra, *Atmos. Chem. Phys.*, *7*, 1503–1522.

Lovett, G. M. (1994), Atmospheric deposition of nutrients and pollutants in North America: An ecological perspective, *Ecol. Appl.*, *4*, 629–650, doi:10.2307/1941997.

McMurry, P. H., and J. C. Wilson (1982), Growth laws for the formation of secondary ambient aerosols-Implications for chemical conversion mechanisms, *Atmos. Environ.*, *16*, 121–134, doi:10.1016/0004-6981(82)90319-5.

Meng, Z., and J. H. Seinfeld (1994), On the source of the submicrometer droplet mode of urban and regional aerosols, *Aerosol Sci. Technol.*, *20*, 253–265, doi:10.1080/02786829408959681.

Miyakawa, T., N. Takegawa, and Y. Kondo (2007), Removal of sulfur dioxide and formation of sulfate aerosol in Tokyo, *J. Geophys. Res.*, *112*, D13209, doi:10.1029/2006JD007896.

Miyakawa, T., N. Takegawa, and Y. Kondo (2008), Photochemical evolution of submicron aerosol chemical composition in the Tokyo megacity region in summer, *J. Geophys. Res.*, *113*, D14304, doi:10.1029/2007JD009493.

NARSTO (2004), *Particulate Matter Assessment for Policy Makers: A NARSTO Assessment*, edited by P. McMurry, M. Shepherd, and J. Vickery, Cambridge Univ. Press, Cambridge, U. K.

Park, K., F. Cao, D. B. Kittelson, and P. H. McMurry (2003), Relationship between particle mass and mobility for diesel exhaust particles, *Environ. Sci. Technol.*, *37*, 577–583, doi:10.1021/es025960v.

Ramanathan, V., et al. (2007), Atmospheric brown clouds: Hemispherical and regional variations in long-range transport, absorption, and radiative forcing, *J. Geophys. Res.*, *112*, D22S21, doi:10.1029/2006JD008124.

Richter, A., J. P. Burrows, H. Nüß, C. Granier, and U. Niemeier (2005), Increase in tropospheric nitrogen dioxide over China observed from space, *Nature*, *437*, 129–132, doi:10.1038/nature04092.

Salcedo, D., et al. (2006), Characterization of ambient aerosols in Mexico City during the MCMA-2003 campaign with aerosol mass spectrometry: Results from the CENICA Supersite, *Atmos. Chem. Phys.*, *6*, 925–946.

Shilling, J. E., et al. (2008), Loading-dependent elemental composition of α-pinene SOA particles, *Atmos. Chem. Phys. Discuss.*, *8*, 15,343–15,373.

Simpson, I. J., N. J. Blake, D. R. Blake, E. Atlas, F. Flocke, J. H. Crawford, H. E. Fuelberg, C. M. Kiley, S. Meinardi, and F. S. Rowland (2003), Photochemical production and evolution of selected C_2-C_5 alkyl nitrates in tropospheric air influenced by Asian outflow, *J. Geophys. Res.*, *108*(D20), 8808, doi:10.1029/2002JD002830.

Streets, D. G., et al. (2003), An inventory of gaseous and primary aerosol emissions in Asia in the year 2000, *J. Geophys. Res.*, *108*(D21), 8809, doi:10.1029/2002JD003093.

Streets, D. G., Q. Zhang, L. Wang, K. He, J. Hao, Y. Wu, Y. Tang, and G. R. Carmichael (2006), Revisiting China's CO emissions after the Transport and Chemical Evolution over the Pacific (TRACE-P) mission: Synthesis of inventories, atmospheric modeling, and observations, *J. Geophys. Res.*, *111*, D14306, doi:10.1029/2006JD007118.

Sugimoto, N., I. Matsui, A. Shimizu, I. Uno, K. Asai, T. Endoh, and T. Nakajima (2002), Observation of dust and anthropogenic aerosol plumes in the Northwest Pacific with a two-wavelength polarization lidar on board the research vessel Mirai, *Geophys. Res. Lett.*, *29*(19), 1901, doi:10.1029/2002GL015112.

Takegawa, N., et al. (2004), Removal of NO_x and NO_y in Asian outflow plumes: Aircraft measurements over the western Pacific in January 2002, *J. Geophys. Res.*, *109*, D23S04, doi:10.1029/2004JD004866.

Takegawa, N., Y. Miyazaki, Y. Kondo, Y. Komazaki, T. Miyakawa, J. L. Jimenez, J. T. Jayne, D. R. Worsnop, J. Allan, and R. J. Weber (2005), Characterization of an Aerodyne aerosol mass spectrometer (AMS): Intercomparison with other aerosol instruments, *Aerosol Sci. Technol.*, *39*, 760–770.

Takegawa, N., et al. (2006a), Evolution of submicron organic aerosol in polluted air exported from Tokyo, *Geophys. Res. Lett.*, *33*, L15814, doi:10.1029/2006GL025815.

Takegawa, N., T. Miyakawa, Y. Kondo, J. L. Jimenez, Q. Zhang, D. R. Worsnop, and M. Fukuda (2006b), Seasonal and diurnal variations of submicron organic aerosol in Tokyo observed using the Aerodyne aerosol mass spectrometer, *J. Geophys. Res.*, *111*, D11206, doi:10.1029/2005JD006515.

Takegawa, N., T. Miyakawa, K. Kawamura, and Y. Kondo (2007), Contribution of selected dicarboxylic and ω-oxocarboxylic acids in ambient aerosol to the *m/z* 44 signal of an Aerodyne aerosol mass spectrometer, *Aerosol Sci. Technol.*, *41*, 418–437, doi:10.1080/02786820701203215.

Takegawa, N., et al. (2009), Performance of an Aerodyne aerosol mass spectrometer (AMS) during intensive campaigns in China in the summer of 2006, *Aerosol Sci. Technol.*, *43*, 189–204, doi:10.1080/02786820802582251.

Turpin, B. J., and H. J. Lim (2001), Species contributions to PM2.5 mass concentrations, Revisiting common assumptions for estimating organic mass, *Aerosol Sci. Technol.*, *35*, 602–610, doi:10.1080/02786820152051454.

van Donkelaar, A., R. V. Martin, and R. J. Park (2006), Estimating ground-level $PM_{2.5}$ using aerosol optical depth determined from satellite remote sensing, *J. Geophys. Res.*, *111*, D21201, doi:10.1029/2005JD006996.

Volkamer, R., J. L. Jimenez, F. SanMartini, K. Dzepina, Q. Zhang, D. Salcedo, L. T. Molina, D. R. Worsnop, and M. J. Molina (2006), Secondary organic aerosol formation from anthropogenic air pollution: Rapid and higher than expected, *Geophys. Res. Lett.*, *33*, L17811, doi:10.1029/2006GL026899.

Wang, G. H., K. Kawamura, S. C. Lee, K. F. Ho, and J. J. Cao (2006), Molecular, seasonal and spatial distributions of organic aerosols from fourteen Chinese cities, *Environ. Sci. Technol.*, *40*, 4619–4625, doi:10.1021/es060291x.

Yao, X., A. P. S. Lau, M. Fang, C. K. Chan, and M. Hu (2003a), Size distributions and formation of ionic species in atmospheric particulate pollutants in Beijing, China: 1. Inorganic ions, *Atmos. Environ.*, *37*, 2991–3000, doi:10.1016/S1352-2310(03)00255-3.

Yao, X., A. P. S. Lau, M. Fang, C. K. Chan, and M. Hu (2003b), Size distributions and formation of ionic species in atmospheric particulate pollutants in Beijing, China: 2. Dicarboxylic acids, *Atmos. Environ.*, *37*, 3001–3007, doi:10.1016/S1352-2310(03)00256-5.

Zhang, Q., M. R. Alfarra, D. R. Worsnop, J. D. Allan, H. Coe, M. R. Canagaratna, and J. L. Jimenez (2005a), Deconvolution and quantification of hydrocarbon-like and oxygenated organic aerosols based on aerosol mass spectrometry, *Environ. Sci. Technol.*, *39*, 4938–4952, doi:10.1021/es048568l.

Zhang, Q., M. R. Canagaratna, J. T. Jayne, D. R. Worsnop, and J. L. Jimenez (2005b), Time- and size-resolved chemical composition of submicron particles in Pittsburgh: Implications for aerosol sources and processes, *J. Geophys. Res.*, *110*, D07S09, doi:10.1029/2004JD004649.

Zhang, Q., D. R. Worsnop, M. R. Canagaratna, and J. L. Jimenez (2005c), Hydrocarbon-like and oxygenated organic aerosols in Pittsburgh: Insights into sources and processes of organic aerosols, *Atmos. Chem. Phys.*, *5*, 3289–3311.

Zhang, Q., et al. (2007), Ubiquity and dominance of oxygenated species in organic aerosols in anthropogenically influenced Northern Hemisphere midlatitudes, *Geophys. Res. Lett.*, *34*, L13801, doi:10.1029/2007GL029979.

Zheng, M., L. G. Salmon, J. J. Schauer, L. M. Zeng, C. S. Kiang, Y. H. Zhang, and G. R. Cass (2005), Seasonal trends in PM2.5 source contributions in Beijing, China, *Atmos. Environ.*, *39*, 3967–3976, doi:10.1016/j.atmosenv.2005.03.036.

D. R. Blake, Department of Chemistry, University of California, Irvine, CA 92697-2025, USA.

Z. Deng, M. Hu, R. Xiao, and T. Zhu, College of Environmental Sciences, Peking University, Beijing 100871, China.

S. Han, Y. Kondo, M. Kuwata, T. Miyakawa, and N. Takegawa, Research Center for Advanced Science and Technology, University of Tokyo, 4-6-1 Komaba, Meguro-ku, Tokyo 153-8904, Japan. (takegawa@atmos.rcast.u-tokyo.ac.jp)

H. Herrmann and D. van Pinxteren, Leibniz Institute for Tropospheric Research, Permoserstrasse 15, D-04318 Leipzig, Germany.

A. Hofzumahaus, F. Holland, and A. Wahner, Forschungszentrum Jülich GmbH, Leo Brandtstrasse, D-52425 Jülich, Germany.

K. Kita, Department of Environmental Science, Ibaraki University, 20101 Bunkyo, Mito, Ibaraki 310-8512, Japan.

Y. Miyazaki, Institute of Low Temperature Science, Hokkaido University, N-19, W-9, Kita-ku, Sapporo, Hokkaido 060-0819, Japan.

N. Sugimoto, National Institute for Environmental Studies, Tsukuba 305-0053, Japan.

Y. Zhao, Air Quality Research Center, University of California, Davis, One Shields Avenue, Davis, CA 95616, USA.